



HAL
open science

An assessment of anisotropic phase-field models of brittle fracture

Jean-Michel Scherer, Stella Brach, Jeremy Bleyer

► **To cite this version:**

Jean-Michel Scherer, Stella Brach, Jeremy Bleyer. An assessment of anisotropic phase-field models of brittle fracture. *Computer Methods in Applied Mechanics and Engineering*, 2022, 395, pp.115036. 10.1016/j.cma.2022.115036 . hal-03668563

HAL Id: hal-03668563

<https://enpc.hal.science/hal-03668563>

Submitted on 15 May 2022

HAL is a multi-disciplinary open access archive for the deposit and dissemination of scientific research documents, whether they are published or not. The documents may come from teaching and research institutions in France or abroad, or from public or private research centers.

L'archive ouverte pluridisciplinaire **HAL**, est destinée au dépôt et à la diffusion de documents scientifiques de niveau recherche, publiés ou non, émanant des établissements d'enseignement et de recherche français ou étrangers, des laboratoires publics ou privés.

An assessment of anisotropic phase-field models of brittle fracture

Jean-Michel Scherer^{a,b}, Stella Brach^b, Jérémy Bleyer^{a,*}

^aLaboratoire Navier, Ecole des Ponts, Univ Gustave Eiffel, CNRS, Cité Descartes, 6-8 av Blaise Pascal, 77455 Champs-sur-Marne, France

^bLMS, CNRS, École Polytechnique, Institut Polytechnique de Paris, 91128, Palaiseau, France

Abstract

In several classes of ductile and brittle materials consisting of different cleavage planes, an orientation dependency of the fracture process is observed. It leads for instance to complex failure behaviours and crack paths in polycrystalline or architected materials. This paper focuses on modeling anisotropy of brittle fracture by means of a variational phase-field approach. More precisely, we study different models including several phase (or damage) variables corresponding to different damage mechanisms. First, we recall a multi-mechanism gradient damage model based on an anisotropic non-local fracture energy. We then consider a model accounting for an anisotropic degradation of the elasticity stiffness tensor. Both types of anisotropies are compared in terms of their influence on analytical homogeneous solutions under uniaxial and biaxial tensile loadings. Weak and strong anisotropies are captured via the chosen multi-mechanism damage framework. The models are implemented numerically by using a finite element discretization. In order to improve numerical performance, we implement an algorithm based on a hybrid direct-iterative resolution of the displacement sub-problem. Accuracy of model prediction is assessed by comparing numerical results to theoretical solutions under uniaxial loading. Benchmark numerical tests on notched and perforated plates highlight the role of material parameters on the fracture anisotropy. Furthermore, both models are able to retrieve zig-zag crack patterns observed in prior numerical and experimental studies. Finally, we discuss the predictions of a model combining both types of anisotropies.

Keywords: Multi-mechanism gradient damage models, Variational phase-field approach to fracture, Anisotropic brittle fracture, Toughness anisotropy

1. Introduction

Anisotropic fracture behaviours are commonly observed in a wide variety of brittle materials such as metals (Riedle et al., 1996; Cook, 2006; Wurster et al., 2012), metal oxides and ceramics (Wu et al., 1995; Azhdari et al., 1998), rocks (Barron, 1971), polymers (Takei et al., 2013), composites (Modniks et al., 2015; Mortazavian and Fatemi, 2015) and architected materials (Nguyen et al., 2017a; Brach et al., 2019; Brach, 2020). The fracture anisotropy of these materials is linked to their nano- or microstructure. In an experimental study, Wu et al. (1995) observed for instance zig-zag crack propagation in spinel (MgAl_2O_4) single crystals. Using double cantilever beams, they imposed a macroscopic crack growth along a $\langle 110 \rangle$ crystal direction. Inside the middle groove, they observed a systematic variation of the crack propagation direction. Instead of propagating along the $\langle 110 \rangle$ direction, the cracks displayed a zig-zag pattern of short cracks on $\langle 100 \rangle$ planes. Recently Takei et al. (2013) observed a similar behaviour in bi-oriented polypropylene sheets, for which they gave

*Corresponding author. J. Bleyer, Laboratoire Navier, 6-8 av Blaise Pascal, Cité Descartes, 77455 Champs-sur-Marne, France, Tel : +33 (0)1 64 15 37 43

Email address: [Jeremy.bleyer@enpc.fr](mailto:j Jeremy.bleyer@enpc.fr) (Jérémy Bleyer)

evidence of directions along which the material does not tear. These zig-zag crack patterns have been attributed to a strongly anisotropic fracture behaviour.

15 Recent development of theoretical (Peerlings et al., 1996; Francfort and Marigo, 1998; Forest, 2009; Poh and Sun, 2017) and computational (Bourdin et al., 2000, 2008; Miehe et al., 2010) gradient damage models have allowed to investigate complex aspects of brittle fracture. Among these, the modelling of brittle fracture anisotropy has gained much attention over the past decade (Hakim and Karma, 2005, 2009; Aslan et al., 2011; Shanthraj et al., 2017; Lindroos et al., 2021). Prior gradient 20 damage models of anisotropic brittle fracture can be divided into two different classes. The first class of models introduces fracture anisotropy by means of an anisotropic non-local fracture energy, while the second class introduces an anisotropic degradation of the stiffness tensor. Within the first class of models, the so-called *second order* models account for an anisotropic non-local fracture energy involving the gradient of damage variable(s) (Clayton and Knap, 2015; Liu and Juhre, 2018; Bryant and Sun, 2018; Quintanas-Corominas et al., 2019; Noii et al., 2020; Rezaei et al., 2021). On the other 25 hand, the so-called *fourth order* models involve the Hessian of the damage variable (Li et al., 2015; Teichtmeister et al., 2017; Kakouris and Triantafyllou, 2018; Li and Maurini, 2019; Nguyen-Thanh et al., 2020; Ma and Sun, 2020; Gerasimov and De Lorenzis, 2022). It was shown that second order models predict a reciprocal surface energy that is convex with respect to the orientation. In the sense 30 of Takei et al. (2013), this convexity characterizes a *weak anisotropy*. To overcome the limitation of second order models to weak anisotropy, fourth order models were introduced. These models can predict a reciprocal surface energy which is non-convex with respect to the orientation. They can therefore capture *strong anisotropy*. However, complex numerical methods are needed in order to ensure the higher degree of continuity of the phase-field variable (Hale et al., 2018). Nevertheless, 35 most of the efforts in the recent literature concentrated on anisotropic brittle fracture models (second and fourth order) based on an anisotropic non-local fracture energy. The second class of models based on an anisotropic stiffness degradation was first studied in local settings (Kachanov, 1958; Chaboche et al., 1995; Lemaitre et al., 2000) and then extended to non-local frameworks by Pijaudier-Cabot and Bažant (1987); Bažant and Pijaudier-Cabot (1988). Lately, this class of models was revisited by 40 Wulfinghoff et al. (2017); Bleyer and Alessi (2018); Fassin et al. (2019); Reese et al. (2021); Görthofer et al. (2021); Li et al. (2021).

Recently, above classes of models were extended to multiphase-field frameworks (Nguyen et al., 2017b; Bleyer and Alessi, 2018). These extensions consider a set of several damage variables, each associated with a different fracture mechanism. Nguyen et al. (2017b) suggested that second order 45 phase-field models accounting for multiple damage mechanisms can achieve both strong and weak anisotropy. This multi-mechanism character prevents the need to resort to a higher-order theory which is required in order to model strong anisotropy if only one damage variable is defined (Li et al., 2015). This is an important result, as higher-order phase-field theories often require C^1 regularity (or higher continuity) and thus involve computationally demanding numerical algorithms (Hale et al., 50 2018). On the other hand, for second-order multiphase-field theories, even if a few additional phase-field variables might be needed, C^0 solutions are sufficient and hence standard numerical methods remain operable.

Anisotropic fracture energy and anisotropic stiffness degradation are hence two efficient ways of introducing anisotropy into the fracture behaviour. Nevertheless, a discussion on the strengths and 55 weaknesses of these approaches is missing in the literature, as well as a comparison of their predictions for benchmark numerical experiments. Finally, to the best of our knowledge, a model combining both type of anisotropies has not been proposed yet.

The objective of this work is thus twofold. First, it aims at developing a framework in which anisotropic stiffness degradation and anisotropic non-local fracture energy can be accounted for sep-

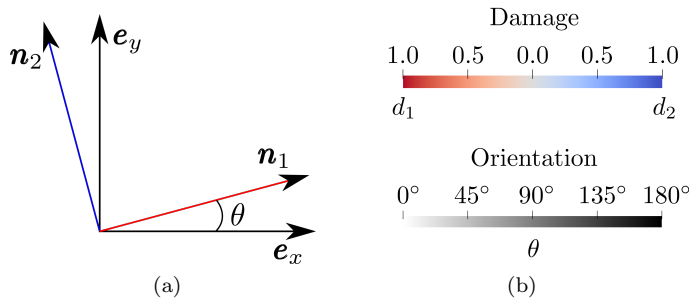


Figure 1: (a) Orientation of the fracture planes of normal \mathbf{n}_1 and \mathbf{n}_2 with respect to the reference basis. (b) Color maps used throughout the paper for the damage variables d_1 , d_2 and the orientation angle θ .

60 arately or simultaneously. Second, it provides a critical assessment of both types of modelling in various anisotropic fracture situations. A second order phase-field fracture model that accounts for multiple damage mechanisms is proposed. The two types of anisotropies are compared in terms of analytical predictions of elastic domains under uniaxial and biaxial tension/compression. The model is then implemented in a finite element framework. The strengths and weaknesses of fracture energy and stiffness degradation anisotropy are discussed on the basis of benchmark numerical tests. Finally, we perform simulations of cleavage fracture in a bi-crystal in order to demonstrate the capabilities of the model to study the fracture behaviour of textured polycrystals.

The article is organized as follows. The theoretical formulation of the model is developed in Section 2. Numerical aspects of the finite element implementation are described in Section 3. Assessment of the implementation and sensitivity of the numerical predictions to material parameters are investigated in Section 4 by performing benchmark numerical tests. Section 5 presents numerical simulations of complex cleavage fracture behaviours in single- and bi-crystals. In Section 6 we revisit previous benchmark numerical tests with a model coupling anisotropies coming from the fracture energy and the stiffness degradation.

75 The following notations are adopted. Vectors and second-order tensors are denoted by boldface symbols. Fourth-order tensors are denoted by blackboard letters. The inner product of second order tensors is denoted by a double dot $\boldsymbol{\varepsilon} : \boldsymbol{\varepsilon} = \varepsilon_{ij}\varepsilon_{ji}$. The dyadic product on vectors is defined by $\mathbf{x} \otimes \mathbf{y} = x_i y_j \mathbf{e}_i \otimes \mathbf{e}_j$, where $\mathcal{R} = \{\mathbf{e}_x, \mathbf{e}_y, \mathbf{e}_z\}$ denotes an orthonormal basis. Damage variables are denoted d_i and evolve from 0 (intact material) to 1 (complete fracture). In this work, we restrict our numerical examples to a 2D plane strain setting and consider only two damage variables d_1 and d_2 for the sake of simplicity. Normal vectors \mathbf{n}_1 and \mathbf{n}_2 define the fracture planes associated to each damage variable. Throughout the paper we will consider that \mathbf{n}_1 and \mathbf{n}_2 are orthogonal. The angle θ defines the orientation of the fracture planes with respect to reference basis as shown in Figure 1a. A red-blue color scale is used for the damage variables and a gray scale is used for the orientation angle θ as described in Figure 1b.

2. Multiphase-field models of anisotropic brittle fracture

In brittle materials, fracture properties might be anisotropic at the scale of the microstructure. In metallic (poly-)crystals for instance, intragranular fracture preferentially occurs along cleavage planes (Pérez and Gumbsch, 2000). Each such cleavage plane i can be defined by its unit normal vector \mathbf{n}_i . In this Section we propose two different ways of accounting for fracture anisotropy due to the existence of cleavage planes.

2.1. Variational phase-field formulation

We formulate here a damage gradient model including several damage variables as in [Bleyer and Alessi \(2018\)](#). The ill-posedness of local damage models is solved by the introduction of a free-energy depending on the damage gradients. Formulated in the standard generalized materials framework ([Halphen and Nguyen, 1975](#)), such models are extremely close to variational phase-field models introduced by [Bourdin et al. \(2000, 2008\)](#). Sharp cracks and displacement discontinuities are regularized via spatially-smooth damage fields $d_i \in [0, 1]$ (with $d_i = 0, \forall i$ for the intact material). According to the generalized continuum thermodynamics framework developed by [Nguyen \(2021\)](#), we consider that the material behaviour can be described by a set of state variables: the linearized strain tensor $\boldsymbol{\varepsilon}$, m different damage variables d_i and their gradients ∇d_i . We assume that the material free energy density depends upon all state variables in the following fashion

$$\psi(\boldsymbol{\varepsilon}, d_i, \nabla d_i) = \psi_{\text{loc}}(\boldsymbol{\varepsilon}, d_i) + \psi_{\text{reg}}(\nabla d_i) \quad (1)$$

where ψ_{loc} denotes the contribution of the local damage model and ψ_{reg} the damage gradient regularizing contribution, both of which will be specified later in [Sections 2.2 and 2.3](#).

As regards the dissipation pseudo-potential, we consider the following rate-independent formulation with respect to the damage rates \dot{d}_i

$$\phi(\dot{d}_i; d_i) = \sum_{i=1}^m f(d_i) \dot{d}_i \quad (2)$$

with the additional irreversibility conditions $\dot{d}_i \geq 0$. Introducing $w(d_i) = \int_0^{d_i} f(u) du$, we have that $f(d_i) = w'(d_i)$ and hence

$$\phi(\dot{d}_i; d_i) = \sum_{i=1}^m \overline{w(\dot{d}_i)} \quad (3)$$

Considering a domain Ω , subjected to body forces \mathbf{b} and surface forces \mathbf{T} on its boundary $\partial\Omega$, the power of external forces is given by

$$\mathcal{P}_{\text{ext}}(\mathbf{v}) = \int_{\Omega} \mathbf{b} \cdot \mathbf{v} \, dV - \int_{\partial\Omega} \mathbf{T} \cdot \mathbf{v} \, dS \quad (4)$$

The system evolution between time t_n and t_{n+1} can be described by the following variational principle

$$\min_{\mathbf{u}, d_i \text{ s.t. } \dot{d}_i \geq 0} \int_{t_n}^{t_{n+1}} \int_{\Omega} \left(\dot{\psi}(\boldsymbol{\varepsilon}, d_i, \nabla d_i) + \phi(\dot{d}_i; d_i) \right) \, dV \, dt - \int_{t_n}^{t_{n+1}} \mathcal{P}_{\text{ext}}(\dot{\mathbf{u}}) \, dt \quad (5)$$

Exploiting expression [\(3\)](#) for the pseudo-potential and simplifying constant terms, we can equivalently write

$$\min_{\mathbf{u}, d_i \text{ s.t. } d_i \geq d_i^n} \int_{\Omega} \left(\psi(\boldsymbol{\varepsilon}, d_i, \nabla d_i) + \sum_{i=1}^m w(d_i) \right) \, dV - \mathcal{P}_{\text{ext}}(\mathbf{u}) \quad (6)$$

where the irreversibility condition has been replaced by $d_i \geq d_i^n$ with d_i^n denoting the previously known value of the damage variables at t_n . The following incremental energy density is introduced

$$W(\boldsymbol{\varepsilon}, d_i, \nabla d_i) = \psi(\boldsymbol{\varepsilon}, d_i, \nabla d_i) + \sum_{i=1}^m w(d_i) \quad (7)$$

We therefore see that the solution at time t_{n+1} can be obtained from the minimization of the following

global incremental pseudo-potential (Bourdin et al., 2000; Petryk, 2003)

$$\min_{\mathbf{u}, d_i} \text{s.t. } d_i \geq d_i^n \int_{\Omega} W(\boldsymbol{\varepsilon}, d_i, \nabla d_i) dV - \mathcal{P}_{\text{ext}}(\mathbf{u}) \quad (8)$$

95 As discussed in (Bleyer and Alessi, 2018) (and references therein) the equilibrium equations, boundary conditions and damage evolution laws can be derived from the optimality conditions of (8). The numerical resolution scheme of the incremental global energy minimization principle will be detailed in Section 3.

2.2. Anisotropic fracture energy

A convenient way to introduce fracture anisotropy into the constitutive modelling of a brittle material is to resort to the use of the second-order structural tensors (Nguyen et al., 2017b)

$$\mathbf{B}_i = \mathbf{1} + \alpha_i(\mathbf{1} - \mathbf{n}_i \otimes \mathbf{n}_i) \quad (9)$$

where α_i is a penalization parameter. Following Bourdin et al. (2000), the incremental pseudo-potential density W introduced in Eq. (8) depends on the elastic strain tensor $\boldsymbol{\varepsilon}$, the damage variables (d_i) and their gradients as follows

$$W(\boldsymbol{\varepsilon}, d_i, \nabla d_i) = \frac{1}{2} \boldsymbol{\varepsilon} : \mathbb{C}(d_i) : \boldsymbol{\varepsilon} + \sum_{i=1}^m \frac{3G_c^i}{8\ell_i} (d_i + \ell_i^2 \mathbf{B}_i : (\nabla d_i \otimes \nabla d_i)) \quad (10)$$

100 where $\mathbb{C}(d_i)$ is the damage-degraded fourth-order stiffness tensor and n the number of different cleavage planes. We introduce the fracture energy density as $\delta(d_i, \nabla d_i) = \sum_{i=1}^m \frac{3G_c^i}{8\ell_i} (d_i + \ell_i^2 \mathbf{B}_i : (\nabla d_i \otimes \nabla d_i))$. Coefficients G_c^i and ℓ_i are the fracture toughness and characteristic length-scale for the fracture mechanism i respectively. In Eq. (10) we have adopted the AT-1 model (Ambrosio and Tortorelli, 1990) instead of the AT-2 model used by Nguyen et al. (2017b). With \mathbb{C}_0 105 the stiffness tensor in the undamaged state, an isotropic elasticity stiffness degradation is introduced as

$$\mathbb{C}(d_i) = \left((1 - \kappa) \prod_{i=1}^m (1 - d_i)^2 + \kappa \right) \mathbb{C}_0 = g(d_i; \kappa) \mathbb{C}_0 \quad (11)$$

where κ is a small residual stiffness introduced in order to avoid ill-posedness in the fully damaged state. In this formulation, the only source of anisotropy comes from the tensors \mathbf{B}_i in the non-local terms of Eq. (10). An isotropic formulation is recovered when $\alpha_i = 0, \forall i$. In Eq. (10), the energetic 110 contribution of gradients of d_i parallel to \mathbf{n}_i does not depend on α_i . However, the energetic contribution of gradients of d_i perpendicular to \mathbf{n}_i scales with $1 + \alpha_i$. Each parameter α_i therefore plays the role of penalizing strain gradients of the variable d_i which are not aligned with the direction \mathbf{n}_i . In the limit of α_i going to infinity, only gradients of d_i strictly aligned with \mathbf{n}_i would be allowed by this model. Parameters α_i enable a direct and scalable control on the degree of anisotropy introduced in 115 the fracture behaviour. However, this also leads to non-straightforward shortcomings, as detailed in Section 4.

We assess the performance of this model via the benchmark problem in Figure 2a (Nguyen et al., 2017b). We consider a plate characterized by a vertical cleavage plane $\mathbf{n}_1 = [1 \ 0]$ and a horizontal cleavage plane $\mathbf{n}_2 = [0 \ 1]$. The damage variables associated with each of these planes are d_1 and d_2 120 respectively. All material parameters are identical for both damage mechanisms, *i.e.* $G_c^1 = G_c^2 = G_c$, $\ell_1 = \ell_2 = \ell$ and $\alpha_1 = \alpha_2 = \alpha$. An isotropic stiffness tensor \mathbb{C}_0 is used. A circular defect of radius

$r_0 = 0.02$ is introduced at the center of the plate by setting either $d_1 = 1$ or $d_2 = 1$. The boundaries of the plate are left free. A sharp damage interface between the defect and the surrounding sound material is not energetically favourable because of the gradient terms in the fracture energy density $\delta(d_i, \nabla d_i)$ in Eq. (10). The minimization of $\int_{\Omega} \delta(d_i, \nabla d_i) dV$, performed with the alternate scheme described in Section 3, results in the damage spreading around the initial defect. Polar plots in Figures 2b and 2c show the normalized fracture energy density δ evaluated at some distance $r > r_0$ as a function of the orientation angle ϕ . For $\alpha = 0$ the fracture behaviour is isotropic. The corresponding fracture energy polar plot is a circle. As α increases, the polar plot of the reciprocal fracture energy density G_c/δ evolves from a convex to a non-convex shape. This result recalls the transition from a *weak anisotropy* to a *strong anisotropy* character. It was argued by Li et al. (2015) that *second-order phase-field* models can only reproduce weak anisotropy, in contrast to *higher-order phase-field* models capable of describing both weak or strong anisotropy. Results shown in Figure 2 suggest that second-order multiphase-field models can also predict both types of anisotropies. As a consequence of this anisotropy, the polar plots of damage variables d_1 and d_2 in Figures 2d and 2e also display an anisotropic profile when $\alpha > 0$. As the parameter α increases, the damage fields are spread over an increased distance around the initial defect.

2.3. Anisotropic elasticity stiffness degradation

Structural tensors \mathbf{B}_i introduced in Section 2.2 are not the only way to model anisotropic failure of brittle materials. The model presented in this Section relies also on Eq. (10), but we assume now that $\mathbf{B}_i = \mathbf{1}$, $\forall i$. In the same spirit as Bleyer and Alessi (2018), we aim at proposing an anisotropic degradation of the stiffness tensor which could be applied to materials having any number of fracture mechanisms. In a 2D setting, with the assumption of two damage planes $\mathbf{n}_1 = [1 \ 0]$ and $\mathbf{n}_2 = [0 \ 1]$, we adopt the following form of the degraded stiffness tensor

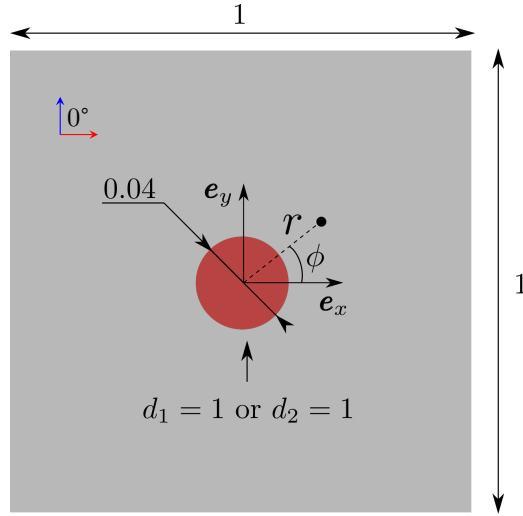
$$\mathbb{C}(d_1, d_2) = \mathbb{D} : \mathbb{C}_0 : \mathbb{D} = \begin{pmatrix} g_1^2 C_{11} & g_1 g_2 C_{12} & 0 \\ g_1 g_2 C_{12} & g_2^2 C_{22} & 0 \\ 0 & 0 & g_6^2 C_{66} \end{pmatrix} \quad (12)$$

$$\text{with } \mathbb{D} = \begin{pmatrix} g_1 & 0 & 0 \\ 0 & g_2 & 0 \\ 0 & 0 & g_6 \end{pmatrix} \quad (13)$$

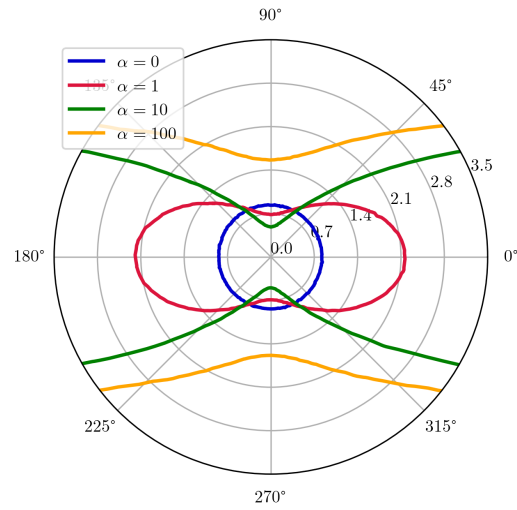
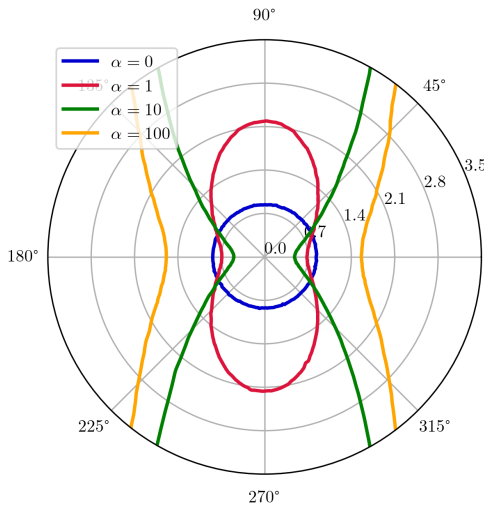
$$\text{and } g_1 = \left(\frac{1 - d_1}{1 + \gamma d_1} \right)^q, \quad g_2 = \left(\frac{1 - d_2}{1 + \gamma d_2} \right)^q, \quad g_6 = \left(\frac{1 - d_1}{1 + \gamma d_1} \right)^p \left(\frac{1 - d_2}{1 + \gamma d_2} \right)^p \quad (14)$$

where \mathbb{D} is an anisotropic degradation tensor. Rational degradation functions g_1 , g_2 and g_6 are adopted (Lorentz and Godard, 2011; Wu, 2017). γ is a material parameter which will be linked to the ratio of two material lengths in Section 2.4. Figure 3 shows the evolution of different degradation functions with respect to damage. On one hand, the rational forms display a faster decrease at incipient damage than the traditional quadratic degradation function. It can therefore be expected that such degradation functions promote crack nucleation. On the other hand, the rational degradation functions display a slow decline towards zero. As a consequence, damaged bands will last longer before evolving into fully developed cracks. The main motivation for Eq. (12) is to account for an *induced anisotropy* of the damaging process. For instance, if $d_2 = 0$ but d_1 evolves from 0 to 1, the material stiffness experiences a strong decrease of its uniaxial and shear components in direction \mathbf{e}_x , while still exhibiting a residual stiffness along direction \mathbf{e}_y parallel to the crack plane.

The degraded stiffness defined in Eq. (12) is restricted to a 2D setting in which only two orthogonal cleavage planes coexist. In an effort to generalize this approach to more general cases, we propose the following formalism. We consider a material with n cleavage planes. For each fracture mechanism,

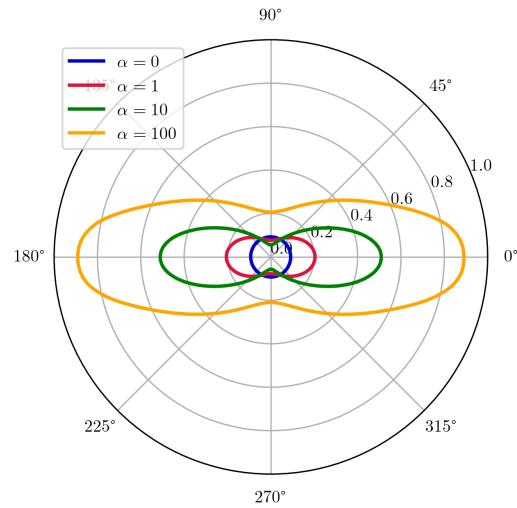
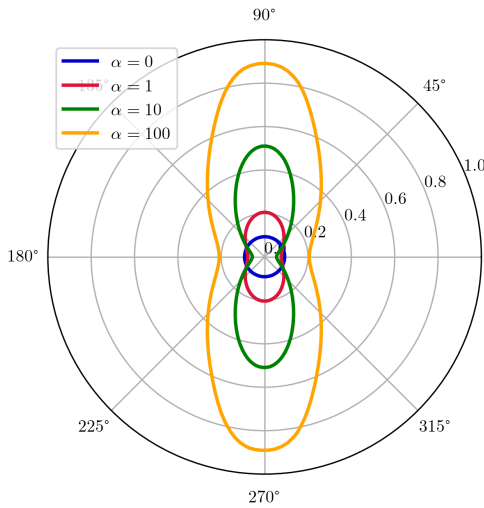


(a) Benchmark problem initial condition



(b) δ/G_c at $r = 0.1$ with $d_1 = 1$ inside the center defect

(c) G_c/δ at $r = 0.1$ with $d_2 = 1$ inside the defect



(d) d_1 at $r = 0.1$ with $d_1 = 1$ inside the defect

(e) d_2 at $r = 0.1$ with $d_2 = 1$ inside the defect

Figure 2: (a) Sketch of the benchmark problem geometry and initial conditions. (b) Polar plots of the normalized fracture energy density δ/G_c , (c) the reciprocal normalized fracture energy density G_c/δ and (d-e) damage level at $r = 0.1$ for the case of a material containing two preferential directions $\mathbf{n}_1 = [1 \ 0]$ and $\mathbf{n}_2 = [0 \ 1]$ with α varying from 0 to 100.

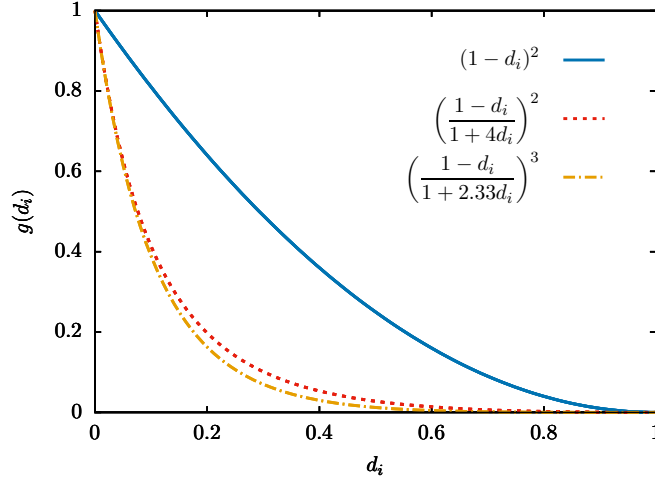


Figure 3: Polynomial and rational degradation functions.

a *residual stiffness tensor* \mathbb{C}_i is introduced. \mathbb{C}_i corresponds to the material stiffness remaining in a crack of plane normal \mathbf{n}_i . In order to describe the smooth transition between the stiffness of the sound material \mathbb{C}_0 and the residual stiffness \mathbb{C}_i of the damaged material, the following non-linear interpolation is introduced

$$\mathbb{C}(d_i) = \left((1 - \kappa) \prod_{i=1}^n g_i(d_i) + \kappa \right) \mathbb{C}_0 + \sum_{i=1}^n \prod_{j \neq i} g_j(d_j) (1 - g_i(d_i)) \mathbb{C}_i \quad (15)$$

150 According to Eq. (15), when only a single damage variable is non-zero (*i.e.* $d_i \neq 0$ and $d_{j \neq i} = 0$), the stiffness evolves from \mathbb{C}_0 to \mathbb{C}_i . The term $\prod_{j \neq i} g_j(d_j)$ is introduced in order to avoid the possibility of artificial stiffness restoration or creation when two cracks coexist at a same material point (*e.g.* at intersection of two cracks). The residual stiffness tensors \mathbb{C}_i can for example be obtained from experiments or computational homogenization (Li et al., 2021).

155 In the following, the abbreviation in Table 1 will be used to denote one or the other of the two models described above. The model with an anisotropic fracture energy is denoted as **AFE**, while the model with an anisotropic stiffness degradation is abbreviated as **ASD**. The Table 1 summarizes the different material parameters for each model. Different sets of values were used for the numerical experiments presented in this study. For each experiment these values are indicated in the Figure captions.

	Anisotropic fracture energy	Anisotropic stiffness degradation
Abbreviation	AFE- α	ASD- (q, p, γ)
Anisotropy parameters	α	γ, p, q
Elastic constants	E, ν	E, ν
Damage parameters	$G_c^1 = G_c^2, \ell_1 = \ell_2$	$G_c^1 = G_c^2, \ell_1 = \ell_2$
Residual stiffness	$\kappa = 10^{-6}$	$\kappa = 10^{-6}$

Table 1: Model abbreviations and material parameters associated to the anisotropic fracture energy and anisotropic stiffness degradation models.

160

2.4. Comparison of homogeneous solutions in uniaxial and biaxial tension

In this section the homogeneous solutions of both models under uniaxial and biaxial tension are compared. The analytical damage initiation criteria are derived and elastic domains are plotted in

order to highlight the differences between the models. We consider a stress tensor taking the following form

$$\boldsymbol{\sigma} = \sigma_{xx} \mathbf{e}_x \otimes \mathbf{e}_x + \sigma_{yy} \mathbf{e}_y \otimes \mathbf{e}_y \quad (16)$$

$$= \begin{pmatrix} \sigma_{xx} \cos^2(\theta) + \sigma_{yy} \sin^2(\theta) & (\sigma_{xx} - \sigma_{yy}) \cos(\theta) \sin(\theta) \\ (\sigma_{xx} - \sigma_{yy}) \cos(\theta) \sin(\theta) & \sigma_{xx} \sin^2(\theta) + \sigma_{yy} \cos^2(\theta) \end{pmatrix}_{(\mathbf{n}_1, \mathbf{n}_2)} \quad (17)$$

where θ represents the angle between the cleavage planes frame $(\mathbf{n}_1, \mathbf{n}_2)$ and the loading frame $(\mathbf{e}_x, \mathbf{e}_y)$ as shown in Figure 1a. It was shown in Bleyer and Alessi (2018), that the damage evolution laws can be expressed as follows

$$\forall i, \begin{cases} Y_i \leq 0 \\ \dot{d}_i \geq 0 \\ \dot{d}_i Y_i = 0 \end{cases} \quad \text{with } Y_i = -\frac{\partial W}{\partial d_i} = \frac{1}{2}(\mathbb{C}^{-1} : \boldsymbol{\sigma})^T : \frac{\partial \mathbb{C}(d_i)}{\partial d_i} : (\mathbb{C}^{-1} : \boldsymbol{\sigma}) - \frac{3G_c^i}{8\ell_i} (1 - 2\ell_i^2 \Delta d_i) \quad (18)$$

Assuming a homogeneous solution, the Laplacian terms Δd_i vanish and the equations $Y_i = 0$ can be interpreted as the equations delimiting the elastic domains associated with each damage mechanism. The intersection of these domains defines the overall elastic domain.

We first consider an initially isotropic stiffness tensor \mathbb{C}_0 , with Young's modulus E and Poisson's ratio ν . In a 2D plane-stress setting, the coefficients C_{11} , C_{22} , C_{12} and C_{66} are expressed in terms of E and ν as follows

$$C_{11} = C_{22} = \frac{E}{1 - \nu^2}, \quad C_{12} = \frac{E\nu}{1 - \nu^2}, \quad C_{66} = \frac{E}{2(1 + \nu)} \quad (19)$$

We define the *elastic limit* σ_0 (Tanné et al., 2018) as

$$\sigma_0 = \sqrt{\frac{3EG_c}{8\ell(1 + \gamma)}} \quad (20)$$

165 It corresponds to the stress at the onset of damage for an homogeneous bar under uniaxial tension. Note that the uniaxial stress might increase above σ_0 in the case of a hardening phase. After the peak stress, softening occurs. For short bars, during the apparent hardening/softening phase, the damage field increases but remains spatially constant. However for long enough bars, the homogeneous solution is unstable in the softening regime and a localized solution is obtained (Tanné et al., 2018).

As discussed in the previous Section, the parameter γ in the degradation functions Eq. (14) can be interpreted as a ratio of two material lengths. We introduce a new cohesive length-scale ℓ_{coh} as follows

$$\ell_{\text{coh}} \equiv \frac{3EG_c}{8\sigma_0^2} = (1 + \gamma)\ell \quad (21)$$

170 Figure 4 shows the elastic domains in uniaxial tension obtained with the AFE model (Figure 4a) and ASD model (Figure 4b). The degradation function parameters are set equal to $p = q = 1$ and $\gamma = 4$. In the case where cleavage planes are aligned with the loading frame (*i.e.* $\theta = 0^\circ$) both models predict a critical nucleation stress equal to σ_0 . For the model AFE accounting for anisotropy in the fracture energy, but having an isotropic degradation of the stiffness tensor, the critical nucleation stress is constant with respect to θ (both damage criteria coincide). However, the model ASD considering an
175 anisotropic degradation of the stiffness tensor yields a non-constant critical nucleation stress. For $\theta \in [0^\circ; 45^\circ] \cup [135^\circ; 180^\circ]$ the damage criterion $Y_1 = 0$ is fulfilled at first, while for $\theta \in [45^\circ; 135^\circ]$ the damage criterion $Y_2 = 0$ is met first. The critical nucleation stress reaches a maximum at $\theta = 45^\circ$ and

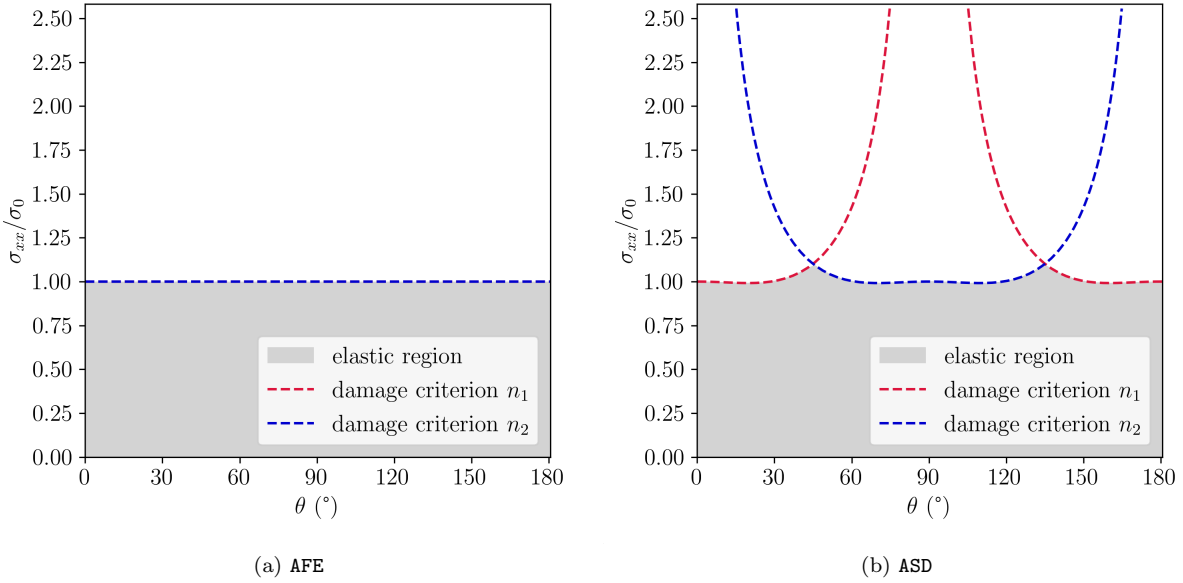


Figure 4: Uniaxial elastic domains for both models with an isotropic stiffness tensor.

$\theta = 135^\circ$.

We further consider an initial stiffness tensor with cubic symmetry, such that the shear modulus $G = C_{66}$ is an independent elastic coefficient. The Zener anisotropy ratio for materials with cubic symmetry is

$$a_r = \frac{2C_{66}}{C_{11} - C_{12}} \quad (22)$$

Zener's ratio is equal to 1 for an isotropic material. Figure 5 shows the elastic domains in uniaxial tension obtained with both models with an initially anisotropic elasticity stiffness tensor. The shear modulus was increased as compared to the isotropic case such that $a_r = 4$. The fracture nucleation stress is no longer constant for the AFE model, but both damage criteria still coincide. The nucleation stress is minimum at $\theta = 0^\circ$, $\theta = 90^\circ$ and $\theta = 180^\circ$ and maximum at $\theta = 45^\circ$ and $\theta = 135^\circ$. For the ASD model, the elastic domain has a similar shape as with the initially isotropic stiffness tensor. The increase of stiffness anisotropy has significantly increased the ratio between the maximum nucleation stress (*e.g.* at $\theta = 45^\circ$) and the minimum nucleation stress (*e.g.* at $\theta = 0^\circ$).

Finally, the elastic domains obtained with both models under biaxial tension with an initially isotropic stiffness tensor are plotted in Figure 6. The cleavage planes are oriented at $\theta = 15^\circ$ with respect to the loading frame. The AFE model leads to an elliptical elastic domain in the $(\sigma_{xx}/\sigma_0, \sigma_{yy}/\sigma_0)$ plane (both criteria coincide). Results not displayed here have shown that the eccentricity of this ellipse increases as the Poisson ratio becomes different from 0. In the limit case where $\nu = 0$ the elastic domain is a circle of radius σ_0 . The ASD model leads to an elastic domain defined by the intersection of two ellipses. The eccentricity of these ellipses increase as Poisson's ratio becomes different from 0. Nevertheless, unlike the previous model, both ellipses do not degenerate to circles when $\nu = 0$. Both models are sensitive to the initial stiffness anisotropy. Increasing Zener's ratio leads to an increase of the eccentricity of the ellipses defining the elastic domains.

3. Numerical implementation

In terms of finite-element discretization, we resort to classical linear Lagrange triangular elements for both the displacement and the damage fields. A standard staggered resolution scheme is adopted

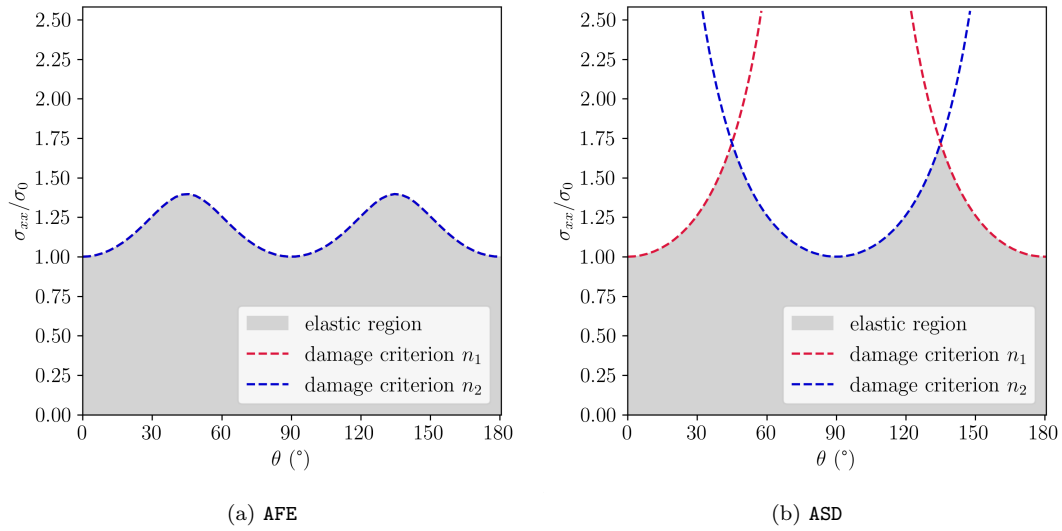


Figure 5: Uniaxial elastic domains for both models with an anisotropic stiffness tensor with $a_r = 4$.

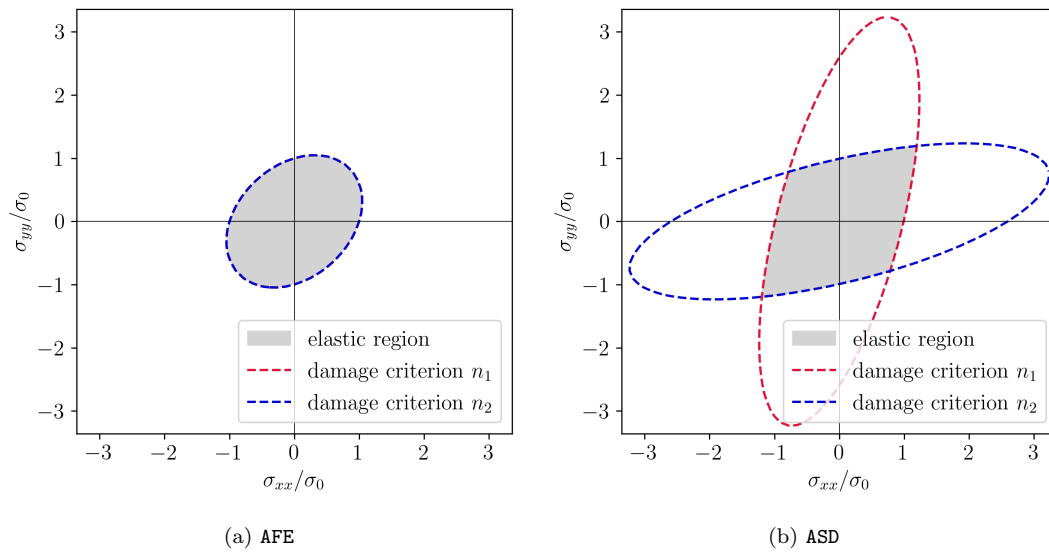


Figure 6: Biaxial elastic domains for both models with $\theta = 15^\circ$ and with an isotropic stiffness tensor.

(Bourdin et al., 2000; De Lorenzis and Gerasimov, 2020) and recalled. Moreover, solving the displacement sub-problem is usually the most time-consuming step of a single alternate minimization iteration. For large-scale problems, direct linear solvers tend to become computationally burdensome. However, devising efficient iterative solvers requires very good preconditioners which are difficult to construct in the presence of strong material non-linearities. As an efficient alternative, we propose in [Appendix A](#) a hybrid direct-iterative method in order to solve the displacement sub-problem.

An incremental minimization of the total energy defined in Eq. (8) is performed. The unknowns of each minimization problem are the displacement and damage variable increments. For a given load increment, denoted by its index n , a fixed-point minimization algorithm is implemented. The convergence criterion is

$$\frac{\mathcal{E}_n^{k+1} - \mathcal{E}_n^k}{\mathcal{E}_n^k} < \varepsilon_{tol} \quad (23)$$

where ε_{tol} is a small tolerance value set equal to 10^{-6} in practice. The indices k and $k+1$ denote two successive iterations of the iterative minimization algorithm. For each iteration k of the fixed-point algorithm, two successive energy minimization are performed. First, energy minimization with respect to the displacement \mathbf{u} is performed with fixed damage variables (d_i)

$$\mathbf{u}_n^k = \underset{\mathbf{u}, \text{ s.t. } (d_i)=(d_i)_n^k}{\operatorname{argmin}} (\mathcal{E}_n^k(\mathbf{u}, d_i)) \quad (24)$$

Then, energy minimization with respect to the damage variables (d_i) is performed with fixed displacement \mathbf{u} , under the constraints of positive damage increments.

$$(d_i)_n^k = \underset{(d_i), \text{ s.t. } \mathbf{u}=\mathbf{u}_n^k}{\operatorname{argmin}} (\mathcal{E}_n^k(\mathbf{u}, d_i)) \quad (25)$$

$$\text{s.t. } \forall i, d_{i,n-1} \leq d_{i,n}^k \leq 1 \quad (26)$$

The resolution with respect to the displacement degrees of freedom \mathbf{u} in Eq. (24) consists in the resolution of a linear variational problem which can be achieved using either a direct method or an iterative method. In [Appendix A](#) a new hybrid method combining both direct and iterative methods is presented. The damage evolution problem Eq. (25) under the constraints of Eq. (26) is solved using the TAO bound-constrained optimization solver (Munson et al., 2012) integrated into the PETSc library (Balay et al., 2001). An adaptive time stepping method is also implemented in order to perform large time steps when damage evolution is inactive and refine the time discretization when damage evolution is active. The full resolution strategy is summarized in Algorithm 1. The open-source software `gradam` developed for this study is based on the FEniCS finite element library (Logg et al., 2012; Alnæs et al., 2015). The source code and implementation of several examples are available at <https://doi.org/10.5281/zenodo.5764329> (Scherer et al., 2021).

4. Numerical experiments: benchmark validation tests

We show that both models presented in Sections 2.2 and 2.3 can give similar predictions for localized cleavage bands under uniaxial tension. The strengths and weaknesses of each model are then discussed via sensitivity analyses to their coefficients. In all these tests, two orthogonal cleavage planes \mathbf{n}_1 and \mathbf{n}_2 are considered. Unless otherwise stated, an initially isotropic elastic behaviour with $E = 200$ GPa and $\nu = 0.3$ is used.

4.1. Comparison of localized solutions in uniaxial tension

225 In order to evaluate the capability of both models to predict crack nucleation on a desired cleavage plane, localized solutions under uniaxial tension are computed. Uniaxial tension along the horizontal direction \mathbf{e}_x is applied to a 2D bar of length $L = 50$ mm along \mathbf{e}_x and width $H = 1$ mm along \mathbf{e}_y . In the following, we consider several orientations θ of the cleavage planes with respect to the loading direction. In order to trigger localization in the center of the bar, a geometrical defect which consists
230 in a width reduction of 1% of the cross-section was introduced.

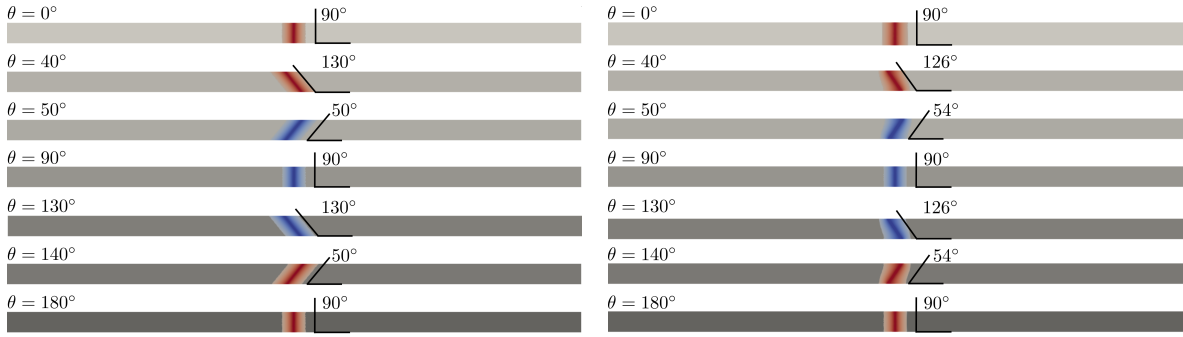
Figures 7a and 7b show the localized solutions obtained with the two different models presented in Sections 2.2 and 2.3. For $\theta \in [0^\circ; 45^\circ] \cup [135^\circ; 180^\circ]$, both models AFE and ASD predict that fracture occurs on the plane of normal \mathbf{n}_1 , while fracture on the plane of normal \mathbf{n}_2 is predicted for $\theta \in [45^\circ; 135^\circ]$. At $\theta = 45^\circ$ and $\theta = 135^\circ$ both damage mechanisms are equivalent, therefore one or the
235 other can be indistinctly activated. However, in these tests both damage mechanisms are never active simultaneously. Furthermore, when cleavage occurs on a given plane the orientation of the localized damage band is not exactly parallel to this plane. The orientation of the localized band particularly depends on the parameter α for the AFE model. In Figure 7c, the evolution of the localized band orientation ϕ with respect to the horizontal direction is plotted as a function of θ . For the smallest
240 value $\alpha > 0$, the orientation of the localized damage band is far from coinciding with the cleavage plane. This is due to the fact that a small value of α only induces a weak anisotropy of the fracture energy (see Figure 2b in Section 2.2). However, as α increases, the orientation of the localization band gets closer to the orientation of the active cleavage plane. The close-up in Figure 7d shows that the orientation of the localized band differs more from the orientation of the cleavage plane when θ
245 is close to 45° . This is the result of a competition between mode I opening (crack perpendicular to the horizontal loading) and crack alignment with the fracture plane. This competition is maximum at $\theta = 45^\circ$ and $\theta = 135^\circ$. The ASD-(1,0.5,4) model, which has an anisotropic stiffness degradation and an isotropic fracture energy, predicts localized band orientations close to the orientations predicted with the AFE-10 model. Additional simulations not presented here have shown that, when the ratio
250 ℓ/H increases, the cracks are still aligned with one or the other cleavage plane in the bulk region away from the edges. For the ASD model, the crack turns from the cleavage plane orientation in the very near vicinity of the top and bottom edges in order to satisfy the free-edge condition. This suggests that both models are indeed potentially well suited for predicting anisotropic fracture on preferential cleavage planes.

255 In Figure 8, we report the total fracture energy (normalized by HG_c) which we interpret as an apparent work of fracture required to break the bar. For $\alpha = 0$, the local fracture behaviour is isotropic and therefore the work of fracture is equal to HG_c in all directions. As α increases, the shape of the work of fracture surface evolves from a circle of radius HG_c to a square of size HG_c . For $\alpha = 100$, at $\theta = 45^\circ$ (diagonal of the square), the work of fracture is equal to $\sqrt{2}HG_c$. Since
260 the corresponding localized damage band is oriented at $\phi = 45^\circ$, the factor $\sqrt{2} = 1/\sin(\pi/4)$ comes from the larger length of the damage band due to this inclination. The surface of (reciprocal) work of fracture obtained with the ASD model displays a similar four fold pattern as obtained with $\alpha > 1$ with the AFE model.

Further numerical tests are presented in the following section in order to highlight the sensitivity
265 of both models to their respective parameters. These tests are also used to emphasize the possible dissimilar predictions obtained from the models.

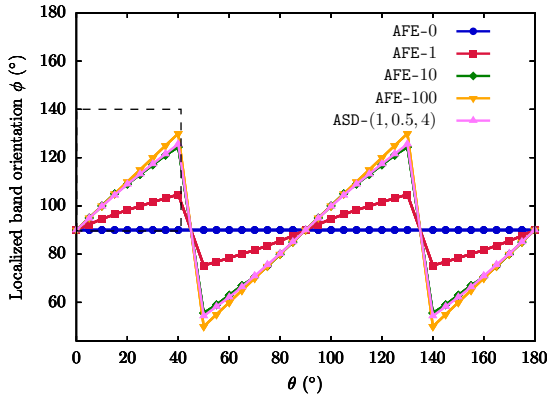
4.2. Mode I loading: $0^\circ/90^\circ$ cleavage planes

Numerical tests are performed on the notched and perforated square plates shown in Figure 9. The plates are loaded in tension by imposing a vertical displacement U to their top edge, while the bottom

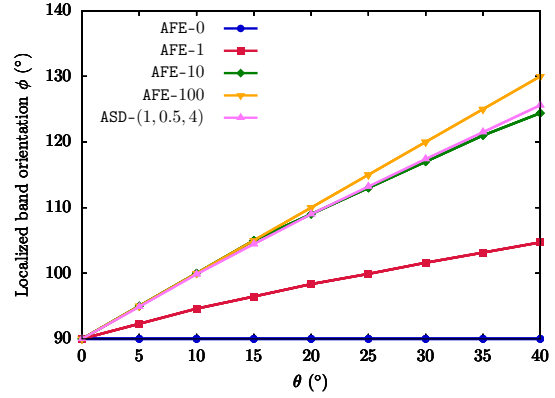


(a) AFE-100 model

(b) ASD-(1,0.5,4) model



(c)



(d)

Figure 7: (a-b) Localized solutions in uniaxial tension for both models with $\mathbf{n}_1 = [1 \ 0]$, $\mathbf{n}_2 = [0 \ 1]$ and $L = 50 \text{ mm}$, $H = 1 \text{ mm}$, $\ell = 0.4 \text{ mm}$. (c-d) Evolution of the localized band orientation ϕ with respect to the fracture planes orientations θ .

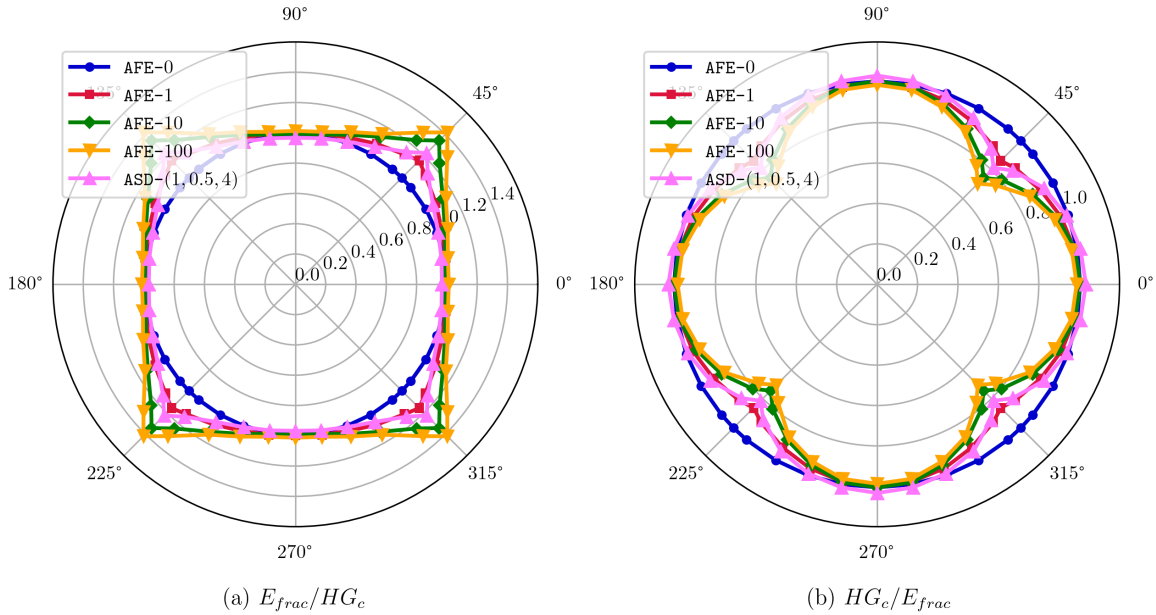
(a) E_{frac}/HG_c (b) HG_c/E_{frac}

Figure 8: Polar plots of (a) the normalized total work of fracture E_{frac}/HG_c and (b) the reciprocal normalized total work of fracture HG_c/E_{frac} for the localized solutions in uniaxial tension.

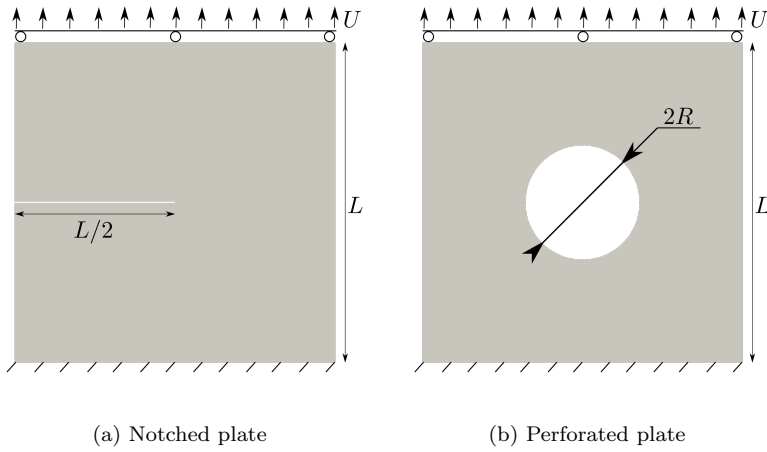


Figure 9: Geometries and boundary conditions on notched and perforated single crystal square plates. $L = 1$ mm and $R \simeq 0.178$ mm such that the void surface fraction is 10%.

270 edge is fixed. The macroscopically applied stress σ_{22} is measured as the applied vertical load (force per unit length) divided by the plate width L . These types of geometries and boundary condition lead to an unstable crack propagation. The corresponding value of the critical stress reached before fracture is therefore denoted σ_c .

First, the case of horizontal straight crack propagation is studied by taking $\theta = 0^\circ$. Due to the vertical loading a crack is nucleated on the plane of normal \mathbf{n}_2 . For the AFE model, the influence of the penalization parameter α is investigated by taking several values in the range $[10^{-2}, 10^3]$. Figure 10 shows the evolution of the critical stress σ_c , normalized by σ_0 as defined in Eq. (20), with respect to α . Horizontal dashed-dot lines represent the normalized critical stress obtained with the ASD model (not sensitive to α). In the weak anisotropy range, *i.e.* $0 \leq \alpha \leq 1$, the critical stress is almost insensitive to the value of α . Furthermore, the critical stress in the limit of vanishing anisotropy ($\alpha \rightarrow 0$) almost coincides with the critical stress predicted by the ASD model. However, in the strong anisotropy range, *i.e.* $\alpha \geq 1$, a significant increase of the critical stress is predicted as α is increased. For the notched plate, σ_c obtained with $\alpha = 10^3$ is more than 2.5 times larger than with $\alpha = 10^{-2}$. Similarly, for the perforated plate, the critical stress is multiplied by about 1.7 between $\alpha = 10^{-2}$ and $\alpha = 10^3$. Moreover it can be observed that for $\alpha = 10^3$ a spurious vertical crack on the cleavage plane of normal \mathbf{n}_1 is initiated at the notch front. The dependency of the predicted crack nucleation stress to the degree of anisotropy is one drawback of the model accounting for a strongly anisotropic fracture energy. The coefficient α which was originally introduced as a penalization parameter without any real physical relevance, seems in fact to play a crucial role in the crack nucleation process. However, the physical interpretation of the coefficient α being still unclear in the literature, the results described above suggest that care should be taken when trying to quantitatively predict critical stresses with a model of this type.

4.3. Mode I loading: $-45^\circ / +45^\circ$ cleavage planes

In Figure 11, the case of a slanted crack propagation in a notched plate is studied by taking $\theta = 45^\circ$. The cleavage plane of normal \mathbf{n}_1 is oriented at -45° with respect to the horizontal axis, while the plane of normal \mathbf{n}_2 is oriented at $+45^\circ$. Since both cleavage planes are orthogonal and the loading applied along the vertical direction, fracture has equal opportunity to occur on one or the other cleavage plane. Figure 11 shows the predictions of the AFE model. The crack paths obtained for three different values of α are superimposed on the notched plate geometry. Consistent with an unstable crack propagation, an elastic-brittle behaviour is observed for all values of α . In case of

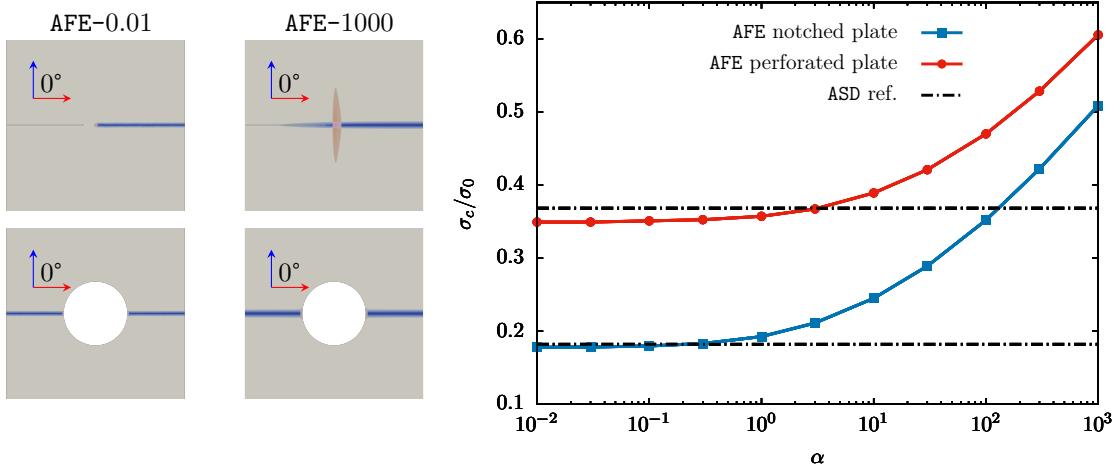


Figure 10: Influence of α on the critical stress to crack nucleation in notched and perforated plates for the AFE model with $\theta = 0^\circ$.

weak anisotropy, *i.e.* $\alpha = 1$, the crack does not fully align with one of the $\pm 45^\circ$ -oriented cleavage planes. This observation is coherent with the localized band orientations measured in uniaxial tension (see Section 4.1). This is the result of a competition between mode I crack opening and the cleavage anisotropy. As α is increased, the cleavage anisotropy becomes dominant. For $\alpha = 100$ the crack propagates exactly along the -45° direction corresponding to the cleavage plane of normal \mathbf{n}_1 . Load-displacement curves of Figure 11 also show that the critical force corresponding to the unstable crack propagation is also highly dependent on α , confirming a previous similar observation. In particular, no convergence seems to be observed when $\alpha \rightarrow \infty$.

Figures 12 and 13 show the predictions of the ASD model. The parameter q is set equal to 1. The crack paths obtained for three different values of p and with $\gamma = 0$ are shown in Figure 12. The parameter p corresponds to the power exponent of the degradation function which acts on the shear modulus (see Eq. (14)). The smaller the value of p , the slower the residual shear modulus drops to zero as damage increases. In fact, increasing the difference between exponents q and p leads to a larger anisotropy of the residual stiffness tensor. The predicted crack paths show that this increased stiffness anisotropy induces a stronger cleavage anisotropy. The crack path tends indeed to get closer to the 45° -oriented cleavage plane when p is decreased. Nevertheless, changing the value of p seems to have relatively little influence on the critical crack nucleation stress. In Figure 13 the power exponents are set to $q = 1$ and $p = 0.5$, while the parameter γ is varied. Increasing the value of γ has the effect of accelerating the decrease of the residual stiffness in the early stages of damage. Therefore, a larger value of γ leads to a greater anisotropy of the residual stiffness. As a result, as observed in Figure 13, when γ is increased, the crack path gets closer to the 45° -oriented cleavage plane.

5. Numerical experiments: complex fracture behaviours

AFE and ASD models are used to simulate crack kinking in elastic orthotropic notched plates. Numerical predictions are compared to a theoretical crack kinking criterion (Leguillon, 1993). Then, we apply surfing boundary conditions (Hossain et al., 2014) to study zig-zag crack propagations in single- and bi-crystal notched plates.

5.1. Crack kinking

Following the work of Amestoy and Leblond (1992) for elastic isotropic materials, Leguillon (1993) developed criteria for predicting crack branching in non-isotropic materials. Recently Bleyer and Alessi

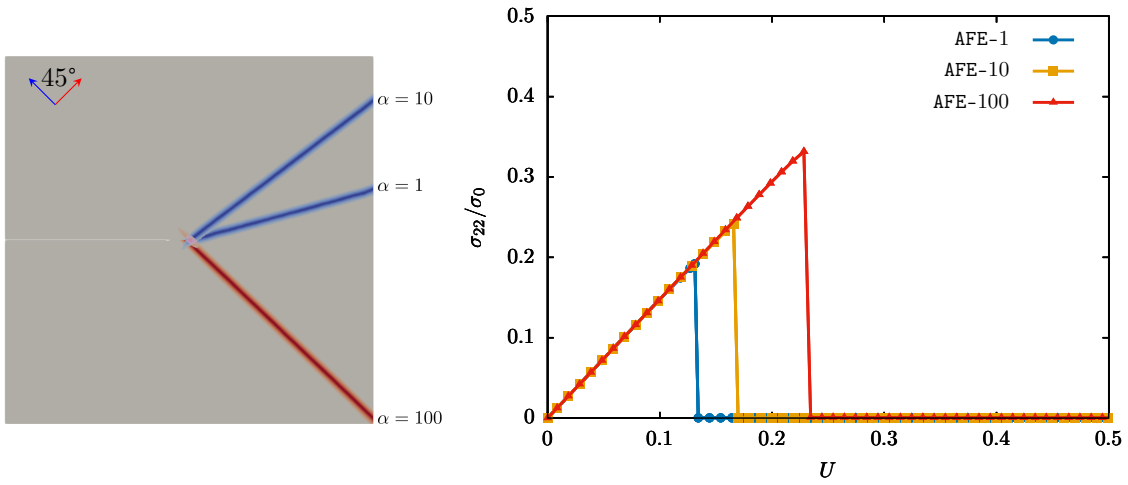


Figure 11: Superimposed crack paths and tensile curves predicted by the AFE model under mode I loading with $\theta = 45^\circ$ and $\alpha = 1, 10$ and 100 .

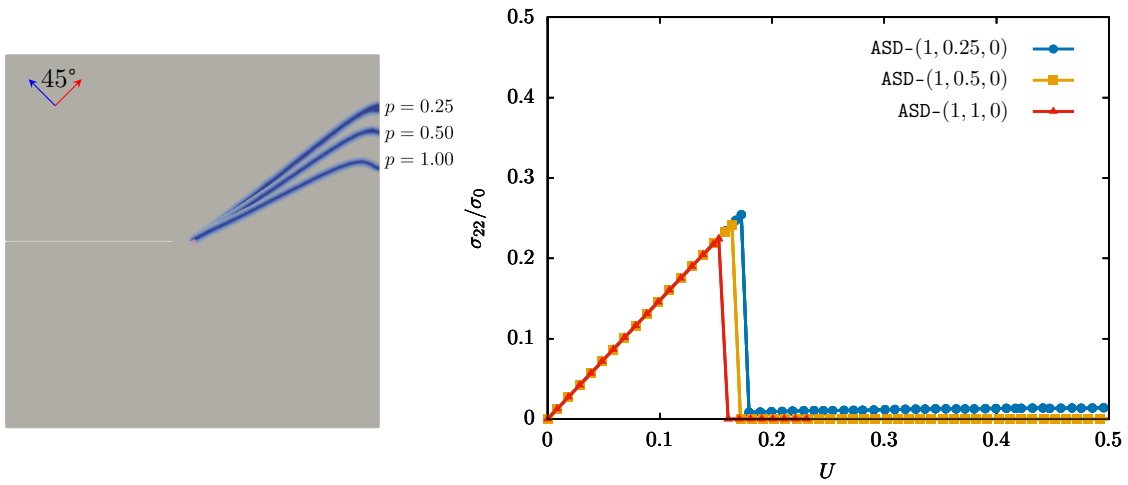


Figure 12: Superimposed crack paths and tensile curves predicted by the ASD model under mode I loading with $\theta = 45^\circ$, $q = 1$, $\gamma = 0$ and $p = 0.25, 0.50$ and 1.00 .

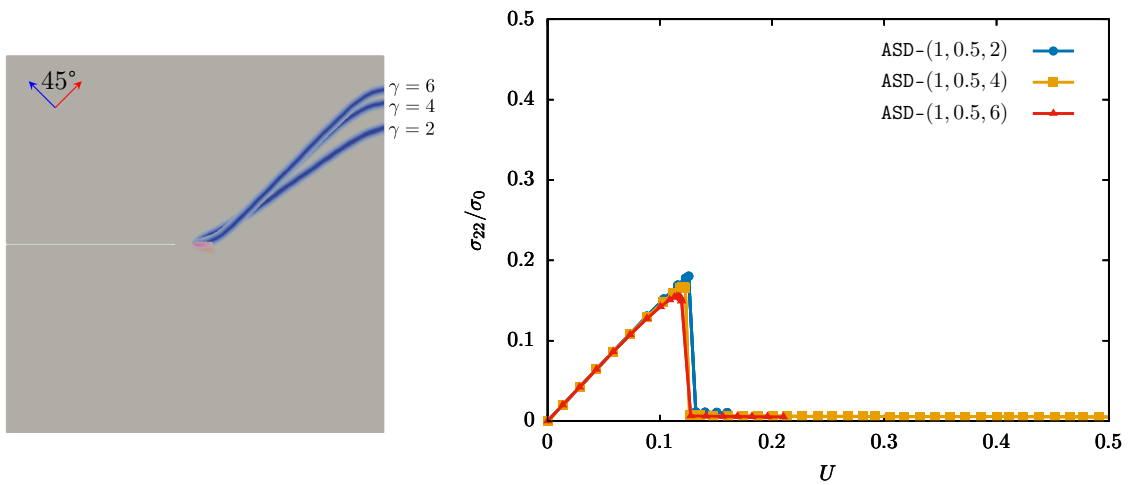


Figure 13: Superimposed crack paths and tensile curves predicted by the ASD model under mode I loading with $\theta = 45^\circ$, $q = 1$, $p = 0.5$ and $\gamma = 2, 4$ and 6 .

(2018) showed that their multi-mechanism gradient damage model accounting for anisotropic stiffness degradation satisfies the crack kinking criterion derived by Leguillon (1993). The same numerical test is reproduced here. This test consists in applying a mode I loading to a sharp crack embedded in an elastically anisotropic material. Leguillon (1993) derived the stress intensity factors (SIF) K_I^* and K_{II}^* of a kinked crack of infinitesimal length

$$K_I^* = F_{11}(\varphi, \beta)K_I \quad \text{and} \quad K_{II}^* = F_{21}(\varphi, \beta)K_I \quad (27)$$

where K_I is the mode I SIF before the kink, while φ represents the kink angle and β the elastic orthotropy direction. The functions F_{ij} depend on φ , β and also on the relative elasticity moduli of the orthotropic medium. The energy release rate can then be expressed as follows

$$G = A_{11}(\varphi, \beta)K_I^2 \quad (28)$$

where A_{11} is obtained from the F_{ij} functions. For a material with an anisotropic fracture energy $G_c(\varphi)$, an extended Griffith criterion states that a crack propagates in a direction φ provided that the condition $G = G_c(\varphi)$ is met. It implies the following minimum principle for the kink angle φ

$$\forall \phi \in [-\pi, \pi], \quad \frac{G_c(\varphi)}{A_{11}(\varphi, \beta)} \leq \frac{G_c(\phi)}{A_{11}(\phi, \beta)} \quad (29)$$

We chose a material with $\beta = \pi/2$, such that the vertical direction is stiffer than the horizontal direction. Two orthogonal cleavage planes $\mathbf{n}_1 = [0 \ 1]$ and $\mathbf{n}_2 = [1 \ 0]$ are considered. The criterion Eq. (29) states that under mode I loading, the crack will kink at $\pm\pi/2$ if the following inequality is met

$$\frac{G_c(\pi/2)}{A_{11}(\pi/2, \pi/2)} \leq \frac{G_c(0)}{A_{11}(0, \pi/2)} \quad (30)$$

With the material parameters considered in Leguillon (1993); Bleyer and Alessi (2018), *i.e.* $E_1 = 142.1$ GPa, $E_2 = 12.4$ GPa, $G = 2.425$ GPa and $\nu_{12} = 0.531$, the ratio $A_{11}(\pi/2, \pi/2)/A_{11}(0, \pi/2) \simeq 0.09$. Therefore, the kinking criterion Eq. (30) will be met if the ratio $\chi = G_c(\pi/2)/G_c(0)$ satisfies

$$\chi = \frac{G_c(\pi/2)}{G_c(0)} = \frac{G_c^2}{G_c^1} \leq \frac{A_{11}(\pi/2, \pi/2)}{A_{11}(0, \pi/2)} = \chi_c \simeq 0.09 \quad (31)$$

The notched plate geometry and boundary conditions of the previous section are used in order to compare the numerical prediction of both models to this analytical criterion. Figure 14 shows the damage fields predicted by the AFE model, with $\alpha = 100$ and $\ell = 0.01$ mm, for several values of χ . A transition of fracture mode occurs for $\chi \in [1, 1.5]$. For the largest value ($\chi = 1.5$) a straight horizontal crack on cleavage plane \mathbf{n}_1 is obtained. As χ is decreased a secondary crack is formed on the cleavage plane \mathbf{n}_2 . For $\chi = 1$ the crack on cleavage plane \mathbf{n}_2 becomes dominant. However, one obtains a diffuse horizontal damage zone, which is far from the picture of a kinked crack in the sense of Leguillon (1993). Moreover, the transition between both fracture modes occurs at values of χ much larger than $\chi_c = 0.09$. This model therefore fails to satisfy the analytical criterion of Leguillon (1993) when $\alpha = 100$.

Figure 15 shows the damage fields predicted by the ASD-(1,0.5,0) model for several values of χ and ℓ . For a characteristic length $\ell = 0.01$ mm, the transition between the straight horizontal crack and the kinked crack occurs at a value of $\chi \in [0.08, 0.15]$ with this model (see Figures 15a, 15b and 15c). At a value of $\chi = 0.1$, *i.e.* slightly above χ_c , the kinked crack becomes vanishingly small as ℓ is decreased (see Figures 15b, 15d and 15e). This suggests that the formation of a kinked crack

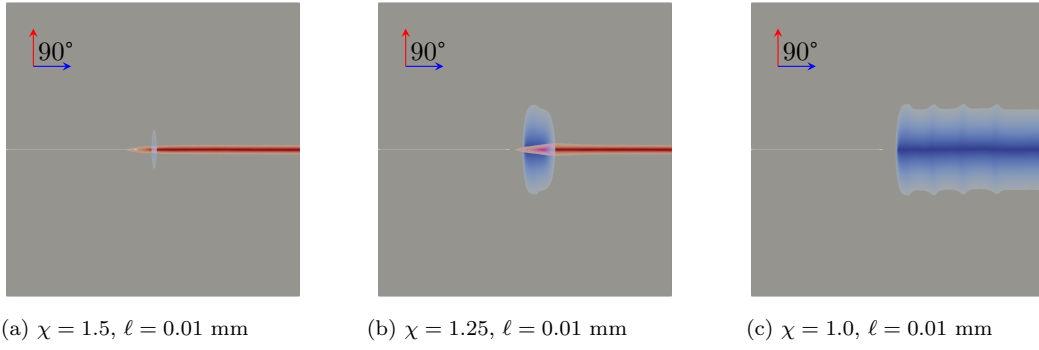


Figure 14: Damage fields obtained with the AFE-100 model as a function of χ .

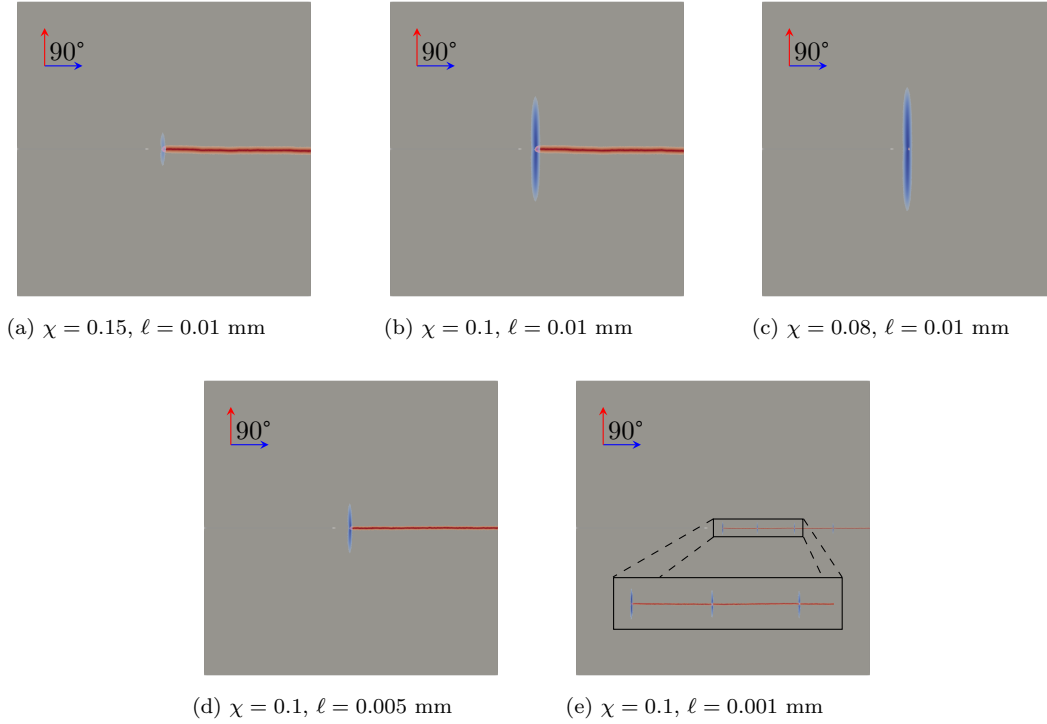


Figure 15: Damage fields obtained with the ASD-(1,0.5,0) model as a function of χ and ℓ .

takes place for a value of χ very close to the theoretical value of χ_c . This result is consistent with the similar conclusions obtained by Bleyer and Alessi (2018) with a closely related model accounting for anisotropic stiffness degradation. In Figure 15e, several secondary crack kinks are observed. The occurrence of such kinks appears to be periodic. In fact, additional simulations, for smaller material length $\ell \in [0.001, 0.005]$, have shown that the distance between to crack kinks is proportional to ℓ .

5.2. Zig-zag crack paths in single crystals

Li et al. (2015); Nguyen et al. (2017a); Li and Maurini (2019); Ma and Sun (2020); Petrini et al. (2021) investigated zig-zag crack propagation (Wu et al., 1995; Takei et al., 2013) via phase-field damage models. Nguyen et al. (2017a); Ma and Sun (2020); Petrini et al. (2021) used a second-order multiphase-field model with an anisotropic fracture energy similar to the model presented in Section 2.2, while Li et al. (2015); Li and Maurini (2019); Ma and Sun (2020) employed a fourth-order phase-field damage model. These studies have shown that models accounting for an anisotropic fracture energy are able to reproduce the phenomenological behaviour of zig-zag cracking. It is therefore

interesting to study if a model accounting for an anisotropic stiffness degradation and with an isotropic fracture energy could also reproduce the same kind of fracture behaviour.

In order to impose a stable crack propagation inside a notched plate, surfing boundary conditions (Hossain et al., 2014) are applied on the boundary

$$\mathbf{u} = \sqrt{\frac{(1+\nu)G_c}{2E}} (3 - 4\nu - \cos\phi) \sqrt{\frac{r}{2\pi}} \left(\cos\left(\frac{\phi}{2}\right) \mathbf{e}_x + \sin\left(\frac{\phi}{2}\right) \mathbf{e}_y \right) \quad (32)$$

where $r(x - v_0t, y)$ and $\phi(x - v_0t, y)$ are polar coordinates (functions of the Cartesian coordinates x and y) at the crack tip, and t is a loading parameter. v_0 corresponds to the imposed macroscopic crack velocity, the crack tip being located at $x = v_0t$ at time t . This boundary condition macroscopically drives propagation along the x -direction with constant velocity v_0 , while the crack is let to freely evolve at the local scale (see also Brach et al. (2019); Brach (2020)). The cleavage plane of normal \mathbf{n}_1 is oriented at -45° with respect to the horizontal axis, while the plane of normal \mathbf{n}_2 is oriented at $+45^\circ$. The outer border of the simulation domain is non-damageable.

The vector \mathbf{j} is introduced as follows

$$\mathbf{j} = \oint_{\mathcal{C}} (\psi_e \mathbf{1} - \nabla \mathbf{u}^T \cdot \boldsymbol{\sigma}) \cdot \mathbf{n} dl \quad (33)$$

where \mathcal{C} is a contour surrounding the crack tip, \mathbf{n} is the outward normal vector to the contour, and ψ_e is the elastic energy density. The J -integral (Cherepanov, 1967; Rice, 1968) is equal to the projection of \mathbf{j} onto the direction \mathbf{t} tangential to the crack tip, that is $J = \mathbf{j} \cdot \mathbf{t}$. At the macroscopic scale of observation, we define the far-field J -integral as the projection of \mathbf{j} onto the prescribed macroscopic path \mathbf{e}_x , that is $J_x = \mathbf{j} \cdot \mathbf{e}_x$. This quantity identifies the macroscopic driving force necessary to sustain crack propagation throughout the material.

In the following, results computed via Eq. (33) are normalized with respect to the numerical fracture toughness $G_c^{num} = G_c(1 + 3h/8\ell)$ (Bourdin et al., 2008), where h represents the mesh size. A measure of the crack length is obtained by computing the normalized fracture energy E_{frac}/G_c^{num} (per unit thickness). In the upcoming figures, solid curves denote the evolution of the far-field J -integral as a function of the applied loading, while shaded ones refer to the evolution of the fracture energy.

Figure 16 shows the crack patterns, the far-field J -integral J_x and fracture energy obtained with the AFE model, for different values of α . For $\alpha = 1$, the crack deflects slightly from the horizontal direction and follows the macroscopically-imposed propagation direction. The corresponding J -integral increases with v_0t until reaching a constant value, slightly larger than G_c^{num} . The fracture energy increases linearly demonstrating the stable propagation of the crack. For $\alpha = 10$, the crack propagates in a slanted direction until it reaches the domain boundary. The crack then gets pinned on the edge, causing the J -integral to increase and to reach more than twice the value of G_c^{num} . At some point, the surfing boundary condition manages to release the crack which then propagates horizontally along the boundary of the domain. The J -integral reaches a plateau value, which is significantly larger than G_c^{num} . In this case, the deflection that the crack would naturally take due to the anisotropy is incompatible with the macroscopically-imposed direction for crack propagation. This competition finally results in the crack propagating in the horizontal direction, but at a significantly higher energetic cost than G_c^{num} . Strong anisotropy with $\alpha = 100$ leads to a zig-zag crack pattern similar to the one obtained by Li et al. (2015); Nguyen et al. (2017a). The crack follows alternatively $\pm 45^\circ$ -oriented cleavage planes. It displays 90° kinks as it interacts with the outer border of the domain. Other simulations performed on wider domains (height equal to $2H$ and $4H$) have shown that this model still predicts crack kinking at the domain boundary. The first peak of the far-field J -integral J_x corresponds to the nucleation of the first crack branch towards the bottom of the domain. Then,

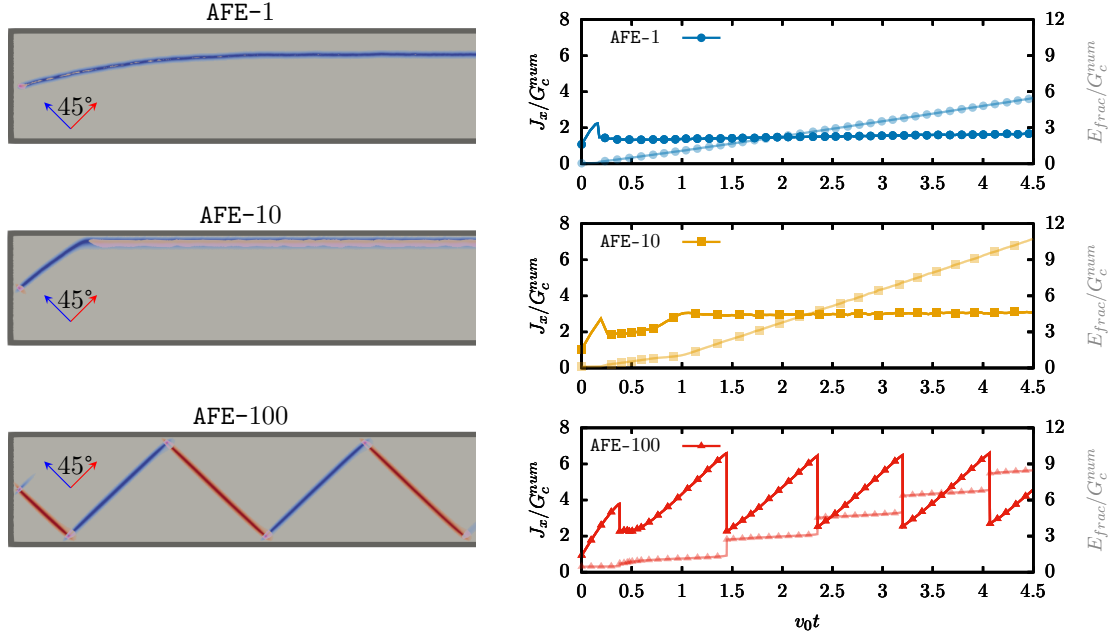


Figure 16: Zig-zag crack obtained with the AFE model as a function of α for $\theta = 45^\circ$.

the far-field energy-release rate increases significantly as the crack remains pinned at the boundary. Once a new unstable crack branch is nucleated, the far-field J -integral instantaneously drops. In fact, every peak of J_x observed for $\alpha = 100$ is due to crack arrests before kinking. value of the J_x after the peak is slightly larger than G_c^{num} . The fracture energy correspondingly displays a discontinuous evolution.

The zig-zag crack pattern and its relation to the evolution of the far-field J -integral in a strongly anisotropic medium can be understood as follows (see also Brach et al. (2019)). Consider a material with strongly anisotropic fracture toughness, and containing a crack oriented at $+45^\circ$ as shown in Figure 17. The red dashed line \mathbf{t}_1 describes the direction of crack propagation associated to the fracture mechanism d_1 . The blue dashed line identifies the propagation direction \mathbf{t}_2 , related to d_2 . The toughness is equal to G_c along the blue and the red paths. This is shown by the blue and red solid lines on the left of Figure 17a. At the point marked 0, the crack is oriented along \mathbf{t}_2 , therefore, under sustained loading, crack propagation proceeds if the condition $\mathbf{j} \cdot \mathbf{t}_2 = G_c$ is fulfilled. As the crack advances, the component of \mathbf{j} along the propagation direction \mathbf{t}_2 has to remain equal to G_c . Hence, the vector \mathbf{j} rotates away from the horizontal direction, from point marked 0 to point marked 1 as shown in Figure 17a. The component of \mathbf{j} along \mathbf{e}_x increases correspondingly. As a result, the far-field J -integral $J_x = \mathbf{j} \cdot \mathbf{e}_x$ increases as the crack deviates from the prescribed macroscopic path, as shown for instance in Figure 16 for $\alpha = 100$.

As the loading proceeds, the J -integral $J = \mathbf{j} \cdot \mathbf{t}_2$ reaches the critical value J^* necessary to activate the fracture mechanism d_1 . Involving the nucleation of a new crack, J^* is strictly larger than the toughness G_c . This is shown as a light-red solid line in Figure 17b. Crack kinking occurs at the point marked 2, where $J = J^*$. The nucleation of the new crack is accompanied by a drop of the far-field J -integral and an instantaneous increase in fracture energy as those shown in Figure 16.

The subsequent stages of propagation are similar to those described above. The crack propagates in the \mathbf{t}_1 direction, for $J = G_c$. The vector \mathbf{j} rotates away from the horizontal direction, in the opposite sense to that observed in Figure 17b. As the loading increases and the crack continues to propagate, the vector \mathbf{j} increases in magnitude following the red solid line. The far-field J -integral J_x correspondingly increases, as shown in Figure 16. Once reached the critical value $J = J^*$ at the point

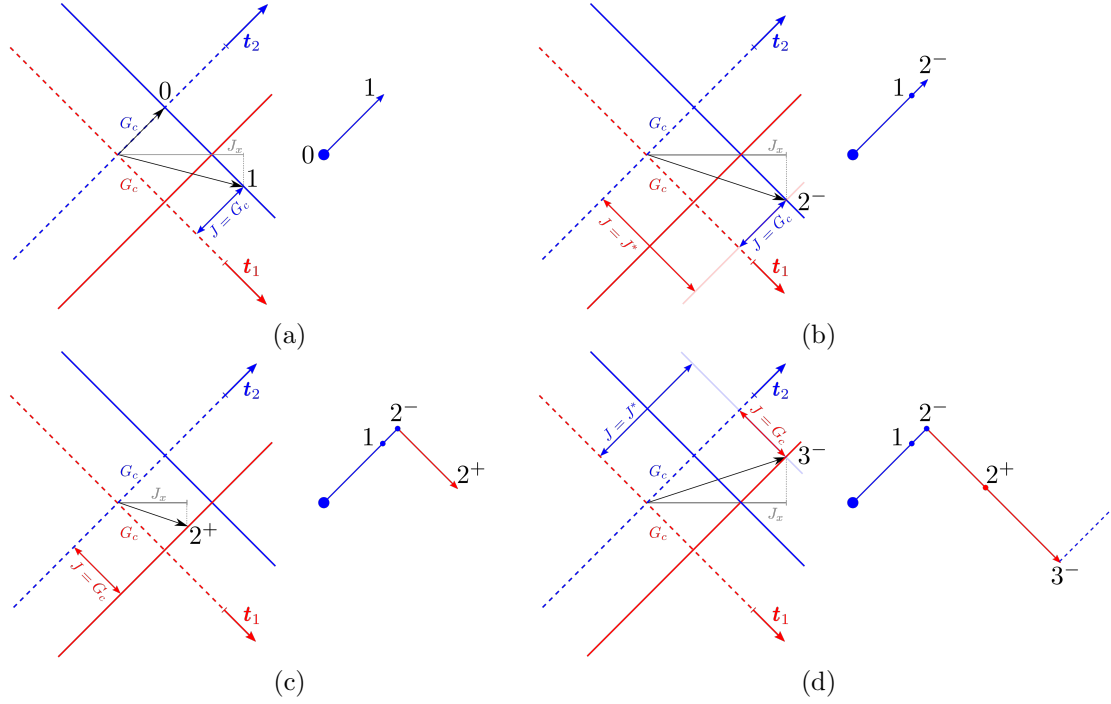


Figure 17: Zig-zag crack paths analysis in a strongly anisotropic medium with two cleavage mechanisms.

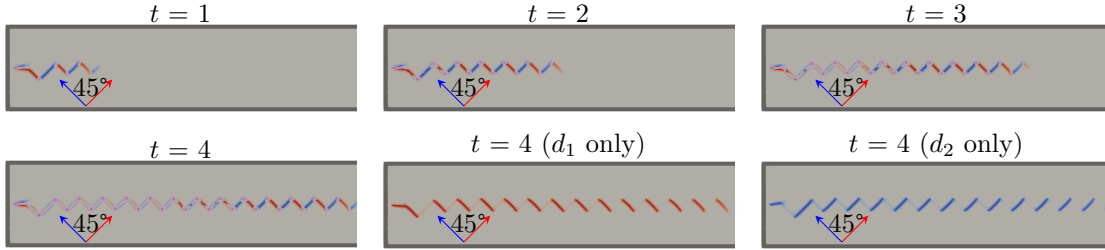


Figure 18: Zig-zag crack history obtained with the ASD-(1,1,4) model at $\theta = 45^\circ$.

marked 3, a new crack is nucleated in the direction \mathbf{t}_2 . The far-field J -integral subsequently drops in Figure 16, accompanied by an instantaneous increase in fracture energy.

As a result, materials with strongly anisotropic toughness display zig-zag crack patterns as those shown in Figure 16. Similar observations, summarized in Figure B.26 of the Appendix, allow to explain crack kinking in weakly anisotropic materials.

Figure 18 shows the history of the crack at several loading steps for the ASD model. Similarly to the case of the AFE model, zig-zag crack patterns are observed. In the first stages of crack propagation, both damage mechanisms are simultaneously active in small regions in the vicinity of kinks. As the crack moves forward, the two damage fields superimpose. On each crack branch, the firstly activated mechanism reaches the maximum value of 1. Meanwhile, the secondly activated damage mechanism always takes relatively limited values ($d \sim 0.1 - 0.2$). This secondary damage activation comes from the non-vanishing residual stiffness remaining within the first crack. In order to eventually reach a fully damaged state (stiffness close to 0), the second damage mechanism is activated with some delay.

A major difference between AFE and ASD models lies in the frequency of crack kinking. While kinking occurred only close to the outer boundary with the AFE model, kinking occurs within the bulk of the domain with the ASD model. Figure 19 shows the crack patterns, far-field J -integral and

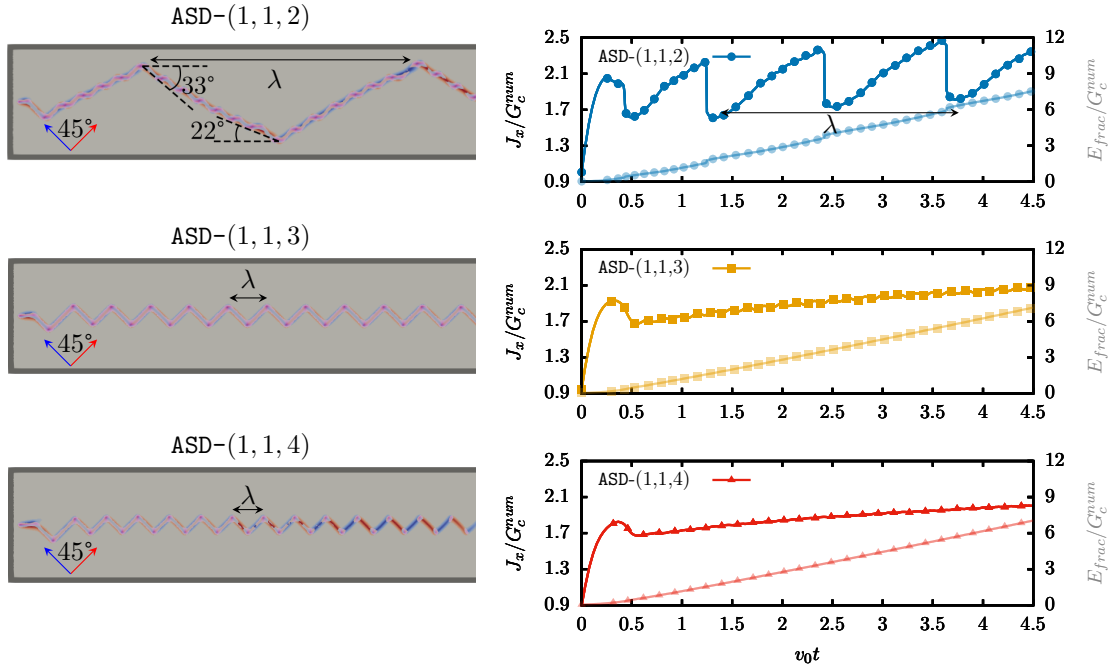


Figure 19: Zig-zag crack obtained with the ASD-(1,1, γ) model as a function of γ for $\theta = 45^\circ$.

fracture energy predicted with the ASD model for several values of parameter γ . For $\gamma = 2$, the far-
 440 field J -integral J_x deviates from G_c^{num} , because the propagation direction progressively bends towards
 the horizontal direction. The crack is oriented at 33° with respect to \mathbf{e}_x just after the second kink.
 Before the third kink it is oriented at 22° . This is due to the fact that $\gamma = 2$ corresponds to the
 weakest anisotropic behaviour (see Figure 15). For $\gamma = 3$ and 4, the far-field J -integral displays lower
 amplitudes of variation, because crack branches experience less deflection than for $\gamma = 2$. However,
 445 J_x slowly decreases after crack nucleation. This is due to the finite size of the computation domain.
 For longer domains, J_x stabilizes to a constant value, equal to the local toughness in the propagation
 direction. For the three values of γ , the fracture energy increases almost linearly with $v_0 t$ showing the
 stable crack propagation.

The zig-zag half period $\lambda/2$ which separates two kinks is strongly correlated to the value of γ .
 450 Increasing γ leads to more frequent kinks. In addition, the period between two kinks depends not
 only on γ , but also on the length scale ℓ . Additional simulations have shown that the half-period
 between kinks $\lambda/2$ is always much larger than the material length ℓ . The ratio between λ and ℓ
 decreases exponentially from two orders of magnitude to one order of magnitude as the ratio ℓ_{coh}/ℓ
 varies between 3 and 6.

5.3. Zig-zag crack paths in bi-crystals

The failure of a bi-crystal consisting of two consecutive grains of identical size is investigated. As
 shown in Figure 20, the notch is located in the first grain of orientation $\theta_1 = 0^\circ$. The second grain
 has an orientation $\theta_2 = 45^\circ$. The imposed surfing boundary conditions lead to an horizontal crack
 propagation in the first grain for both models. However, as the crack front approaches the interface
 460 between the two grains it starts to interact with the second grain. The AFE model predicts a straight
 horizontal crack up to the grain boundary. In contrast, the ASD model predicts a slightly slanted crack
 path ahead of the interface. During the crack propagation in the crystal oriented at $\theta_1 = 0^\circ$, both
 models display a similar evolution of the far-field J -integral. Its value is almost constant and close to
 G_c^{num} as expected for a mode I crack propagation. The fracture energy is larger for the AFE model
 465 than for the ASD model, because the former predicts a wider cracked region than the latter. However,

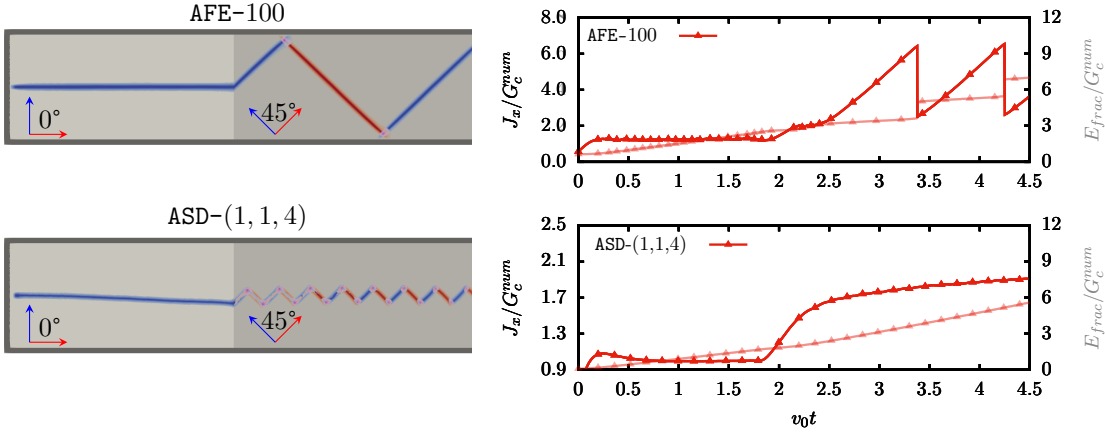


Figure 20: Crack path inside a bi-crystal obtained with the AFE-100 and ASD-(1,1,4) models for $\theta_1 = 0^\circ$ and $\theta_2 = 45^\circ$.

both models predict similar slopes of the fracture energy evolution. The crack tip velocity is therefore comparable between the two models during stable crack propagation in the 0° -oriented grain. As the crack crosses the grain boundary, AFE and ASD predictions differ significantly. Crack patterns, far-field J -integral and fracture energy observed in the grain oriented at $\theta_2 = 45^\circ$ are similar to those observed for single crystals in Section 5.2. With the AFE model, the large value of α used in this example leads to crack branches oriented at $\pm 45^\circ$. However, results obtained with this model strongly depend on the penalization parameter. The J -integral peaks and fracture energy jumps are due to crack pinning at the boundary. The ASD model, on the contrary, predicts crack kinking before the crack reaches the boundary. The J -integral reaches a constant value and predicted results do not depend on the size of the computation domain.

6. A model combining fracture energy and stiffness degradation anisotropies

In previous Sections, we discussed the formulation and numerical predictions of models accounting either for anisotropic fracture energy (AFE) or anisotropic stiffness degradation (ASD). The AFE model effectively enforces the direction of the fracture process, as cracks propagate along the prescribed cleavage direction. The crack nucleation stress was shown to strongly depend on the penalization parameter α . No convergence of the crack nucleation stress was reached even for very large values of α (see Figure 10). Moreover, the AFE model with large value of α predicted extended damage zones instead of expected crack kinks in elastic orthotropic materials. The ASD model, on the contrary, does not strictly impose the direction of crack propagation. However, it accurately predicts crack kinking and shows a very good agreement with the criterion of Leguillon (1993). Here, we combine the two models and analyze the performance of the coupled formulation, denoted as AFS- (α, q, p, γ) .

Figure 21 shows the superimposition of crack paths in a notched plate in tension with the AFS model for several values of α . As expected, the resulting model displays a greater degree of anisotropy than when only one source of anisotropy or the other is individually accounted for. Nevertheless, the dependence of the crack nucleation stress to α remains a main drawback of this combined model.

As regards the crack kinking problem, the AFS model tends to be in better agreement with Leguillon's crack kinking criterion than the AFE model. With $\alpha = 100$, $q = 1$, $p = 0.5$ and $\gamma = 0$, Figure 22 shows that crack kinks similar to those obtained with the ASD model in Figure 14 are observed for $\chi < 0.25$. However, this value is more than twice the value predicted by Leguillon's criterion ($\chi_c \simeq 0.09$ for the material parameters considered in Section 5.1). Note that the AFE model is found unable to predict expected crack kinks, but predicts wide diffuse damage zones instead. Furthermore,

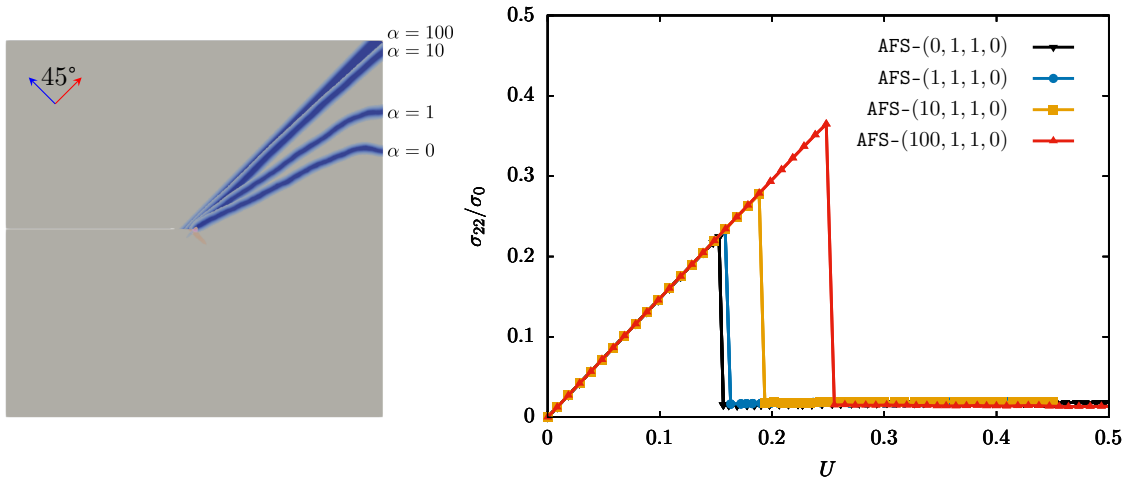


Figure 21: Superimposed crack paths and tensile curves predicted by the AFS model under mode I loading with $\theta = 45^\circ$, $q = 1$, $p = 1.0$, $\gamma = 0$ and $\alpha = 0, 1$ and 10 .

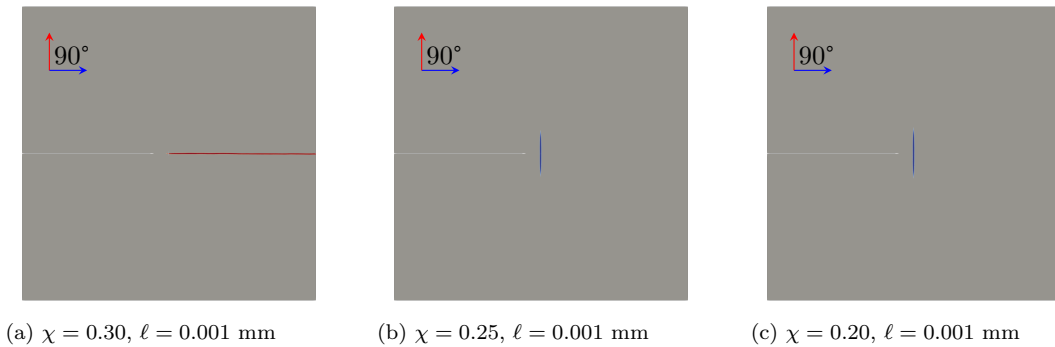


Figure 22: Damage fields obtained with the AFS-(100,1,0.5,0) model as a function of χ .

it can be noted from Figure 21 that, for $\alpha = 10$ and $\alpha = 100$, the AFS model anisotropies are similar since predicted crack propagation directions are close to 45° for both these values of α . However, additional simulations with $\alpha = 10$ have shown that crack kinks are predicted for $\chi < 0.135$ which is even closer to the theoretical value. Nevertheless, the influence of α on crack kinking remains a main drawback of the penalization method.

The predictions of the AFS model for the notched single crystal and bi-crystal plates under surfing boundary conditions are presented in Figure 23. Far-field J -integral and fracture energy results obtained with the ASD model on the same microstructures (see Figures 19 and 20) are denoted with dashed lines. The fracture patterns obtained with the AFS model are essentially similar to the patterns obtained with the AFE model (see Figures 16 and 20). The crack propagates in a zig-zag fashion, where each branch is oriented at $\pm 45^\circ$. Nevertheless, a major difference lies in the crack propagation stability and kinking occurrences. While the AFE model predicted crack pinning at the boundary and unstable crack jumps upon crack release, the AFS model predicts a linear increase of the fracture energy which denotes stable crack propagation similarly to the ASD model (see Figure 19). Furthermore, adding an anisotropic stiffness degradation to the anisotropic fracture energy model promotes the formation of kinks. It results that crack kinking occurs in the bulk of the material instead of occurring at the outer boundary of the simulation domain.

The first peak in the far-field J -integral J_x corresponds to the nucleation of the crack. The following peaks are associated to kinking events. In the bi-crystal microstructure, the crack propagates first

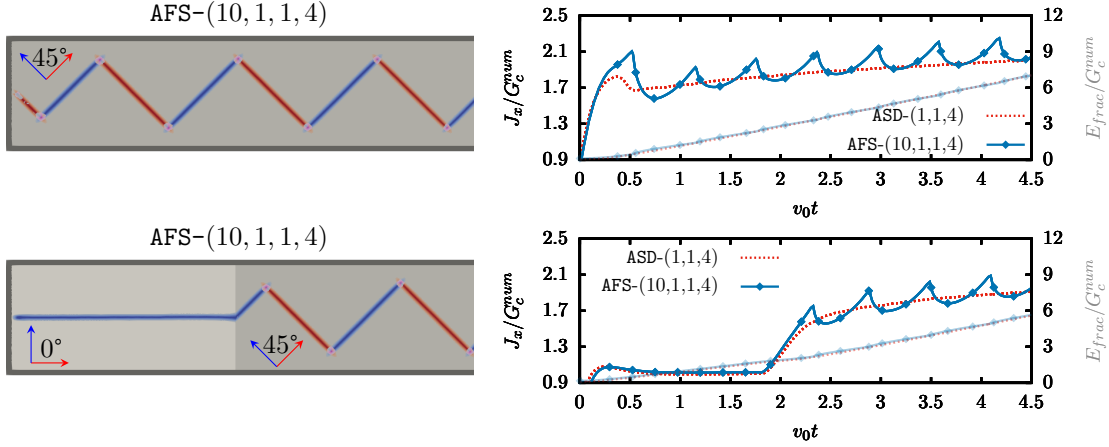


Figure 23: Crack path inside a single and bi-crystal obtained with the AFS-(10,1,1,4) model for $\theta_1 = 0^\circ$ and $\theta_2 = 45^\circ$.

horizontally in the 0° -oriented crystal. As a result, J_x remains almost constant and close to G_c^{num} . When it reaches the 45° -oriented grain, the far-field J -integral follows a similar evolution as for the 45° -oriented single crystal. Since the crack kinks before getting pinned at the domain boundary, the amplitude of J_x variations is much lower with the AFS model than with the AFE model (see Figures 16 and 20). For identical parameters in the degradation functions ($p = 1$, $q = 1$ and $\gamma = 4$), but with $\alpha = 0$, the ASD model predicted an almost constant value of the J_x close to $1.8G_c^{num}$ (see Figure 19).

Although the crack patterns obtained with ASD and AFS models are very different, their predicted J -integrals and fracture energies evolution are very close. To some extent, the ASD model can therefore benefit from the α -penalization in order to strictly enforce cleavage on predefined planes without altering much the far-field energy release rate and dissipated fracture energy. Furthermore, the AFS model does not suffer from simultaneous activation of both damage mechanisms over large areas as it is the case for the ASD model (see Figure 18).

7. Conclusion and perspectives

In this paper, we compare two different approaches to model anisotropy of brittle fracture, by using a variational phase-field formulation. A first model (AFE) introduces anisotropy in the non-local fracture energy (Clayton and Knap, 2015; Nguyen et al., 2017b). In the second formulation (ASD), anisotropy is introduced in the elastic energy via an anisotropic stiffness degradation (Bleyer and Alessi, 2018). The numerical implementation involves a newly developed hybrid method to solve the displacement problem in a direct-iterative fashion within an alternate minimization scheme. In Section 4.1, we showed that both models are able to describe a *strong anisotropy* in the sense of non-convexity of the fracture energy with respect to the material orientation (Takei et al., 2013; Li and Maurini, 2019). However, the anisotropic behaviour predicted by these models is strongly sensitive to the choice of material parameters. In Section 5.1, we show that for a large anisotropy penalization coefficient, the AFE model accounting for an anisotropic fracture energy cannot retrieve theoretical predictions on crack kinking in elastically anisotropic materials (Leguillon, 1993). On the contrary, the ASD model accounting for anisotropic stiffness degradation satisfies the theoretical criterion. In Section 5.2, we assessed the performance of both models in reproducing complex crack patterns. Both models are shown to be able to capture the phenomenology of zig-zag propagation. Yet, the model with anisotropic fracture energy predicts crack kinking at the outer boundary of the computation domain, while the frequency of kinking is adjustable in the case of the model with anisotropic stiffness

degradation. The frequency of crack kinks increases with the degree of anisotropy. Finally, the AFS model combining both types of anisotropies was introduced. It predicts similar crack patterns as the AFE model. However, since anisotropic stiffness degradation promotes kinking, cracks predicted with the AFS model change direction before getting pinned at the domain boundary. As a result, far-field energy-release rate and fracture energy predicted with the AFS model are close to the ASD model predictions.

The two models implemented in this work open the way for future studies, as anisotropic fracture is ubiquitous in engineering applications. Examples include brittle metallic alloys, fiber-reinforced polymers and architected materials. Anisotropic fracture models can help understanding the relationship between microstructure and fracture processes. In the end, such models can contribute to the design of materials which leverage the effect of microstructural features, such as texture or architecture, in order to tailor the fracture behaviour and respond to engineering needs.

Appendix A. Hybrid direct-iterative resolution of the displacement sub-problem

A hybrid direct-iterative resolution method is proposed for the resolution of the linear variational displacement sub-problem. A preconditioned iterative conjugate gradient (PCG) descent method is used as the main linear solver. However, the quality of an initial preconditioner rapidly deteriorates with the evolution of material non-linearities (*e.g.* as the damage variables evolve). As a result, the number of iterations in the conjugate gradient (CG) descent can become prohibitively large or the method can even diverge in some cases. To prevent such poor convergence performances, the preconditioner needs to be frequently updated.

Conversely, relying on a direct solver using LU or Cholesky factorization is much more robust but more time and memory consuming for large-scale linear systems. However, it is often the most practical solution for strongly non-linear mechanical problems which do not benefit from efficient preconditioners.

For a given linear system, the best preconditioner available is obviously the matrix inverse itself. The hybrid direct-iterative strategy that we consider here uses a direct solve at a given time step to obtain a good preconditioner for the subsequent time step. Indeed, we assume that between two time steps, although the linear operator has changed, the inverse at the previous time step remains a good estimate for the current time step. Doing so, we can reuse a single preconditioner computed from the matrix factorization obtained from a previous direct solve for a few subsequent time steps solved using the PCG method. In practice, the quality of this preconditioner will deteriorate after a few time steps, which can be observed through the increase of the number of CG iterations. At some point, a new direct resolution is necessary in order to restore the preconditioner accuracy. The only parameter of the proposed technique is the frequency at which a preconditioner update must be performed. Instead of doing a periodical update, we propose to perform a new direct resolution and preconditioner update each time the number of CG iterations exceeds a critical number noted M in Algorithm 1. If this integer is taken equal to 0, then only direct resolutions are performed. If this integer is strictly positive, preconditioner updates will only be performed when the number of gradient descent iterations is greater than this threshold (*i.e.* when the quality of the preconditioner deteriorates). The hybrid strategy described above is summarized in Algorithm 1.

The optimal value of the iteration threshold M giving the best computational performances is not universal and depends mostly on the size of the linear system. In order to get a better understanding on the role of this parameter, a numerical test is performed on a notched trapezium structure loaded in mode I crack opening as shown in Figure A.24. The trapezium shape is chosen in order to ensure a stable crack growth (Lorentz and Godard, 2011). Two cleavage planes with normals $\mathbf{n}_1 = [1 \ 0]$ and $\mathbf{n}_2 = [0 \ 1]$ are considered. The model ASD-(1,0.5,4) is used in this numerical example. The

Algorithm 1 Staggered numerical scheme involving a hybrid direct-iterative resolution of the displacement sub-problem and adaptive time-stepping

```

1:  $t_0 = 0$  and  $n = 1$ 
2:  $t_n = t_0$ 
3: while  $t_n < T$  do
4:    $dt = \max(dt \times \text{desired\_d\_increment} / \text{previous\_max\_d\_increment}, \text{min\_dt})$ 
5:    $dt = \min(dt, \text{max\_dt})$  ▷ adaptative time stepping with  $\text{min\_dt} \leq dt \leq \text{max\_dt}$ 
6:    $t_n = \min(t_n + dt, T)$ 
7:    $k = 0$  and  $\text{u\_iterative\_counter} = 0$ 
8:   while  $(\mathcal{E}_n^{k+1} - \mathcal{E}_n^k) / \mathcal{E}_n^k \geq \varepsilon_{\text{tol}}$  do
9:     % Solve for  $\mathbf{u}_n^{k+1}$  at  $(d_i)_n^k$  fixed
10:    if  $\text{u\_iterative\_counter} < M$  then
11:      Compute  $\mathbf{u}_n^{k+1}$  with an iterative resolution (PCG method with preconditioner  $[P]$ )
12:       $\text{u\_iterative\_counter} = \text{number of CG descent iterations}$ 
13:    else
14:      Compute  $\mathbf{u}_n^{k+1}$  with a direct resolution
15:       $\text{u\_iterative\_counter} = 0$ 
16:      preconditioner update  $[P] = [A^{-1}]$ 
17:    end if
18:    Compute  $\mathcal{E}_n^k$ 
19:    % Solve for  $(d_i)_n^k$  at  $\mathbf{u}_n^k$  fixed
20:    Apply PETSc TAO solver with the constraints  $\forall i, (d_i)_{n-1} \leq (d_i)_n^k \leq 1$ 
21:    Compute  $\mathcal{E}_n^{k+1}$ 
22:     $k = k + 1$ 
23:  end while
24:   $\mathbf{u}_n = \mathbf{u}_n^k$  and  $(d_i)_n = (d_i)_n^k$ 
25:  Compute  $\text{previous\_max\_d\_increment}$ 
26:   $n = n + 1$ 
27: end while

```

geometry is meshed with 2×10^6 2D-triangular bilinear finite elements with 4 degrees of freedom per node u_1 , u_2 , d_1 and d_2 . The total number of degrees of freedom is 4×10^6 . Crack propagation is driven in the horizontal direction by imposing anti-symmetric displacement boundary conditions on the left edges of the trapezium above and below the notch. Computations are performed on a parallel computer using 48 CPUs.

The numerical test is performed with four different values of the threshold M , namely 0, 5, 10 and 50. The value of 0 corresponds to the situation when only direct resolutions are performed. This case is therefore referred to as "Direct" in Figures A.24 and A.25. A normalized load is computed as the resultant force on the top edge divided by the length of the edge h and divided by σ_0 computed with the same definition as in Eq. (20). Figure A.24 shows the evolution of the normalized load as a function of the displacement. The two algorithms predict the exact same solution regardless of the value of M . However, Figure A.25a shows that the hybrid iterative-direct method outperforms the direct method considerably in terms of normalized computation wall time. The speedup reaches up to a factor 2.5 between the hybrid method with $M = 5$ and the direct method. In Figure A.25, symbols indicate the occurrence of a preconditioner update, *i.e.* when conjugate gradient descent iterations exceeded the value of M . The number of such updates is larger when M is small. One could hence expect the computation time to decrease when increasing M , because a fewer computationally expensive matrix inversions are needed. Yet, the computation time is the lowest for the smallest value of M . This can be explained from the much lower cumulative number of conjugate gradient descent iterations required when $M = 5$ compared with $M = 10$ or 50. As shown in Figure A.25b performing preconditioner updates very often allows to keep the number of iterations of the iterative method rather small. For $M = 5$, the total number of load increments is 1370 and the cumulative number of fixed-point

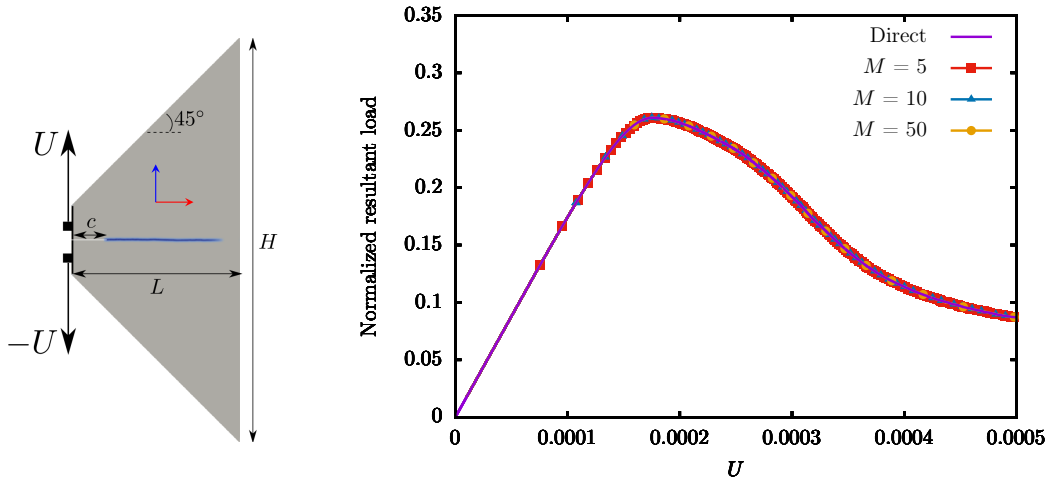


Figure A.24: (a) Geometry of the trapezium structure loaded in mode I and resulting stable crack path. The dimensions of the trapezium are $L = 5$ mm, $H = 12$ mm and the notch length is $c = 1$ mm. (b) Evolution of normalized resultant load *vs* displacement imposed to the trapezium ends obtained with direct and hybrid resolution strategies. The regularization length scale is equal to $\ell = 0.02$ mm and the cleavage energy is $G_c = 10^{-3}$ J/m² for both damage mechanisms. Isotropic elasticity is considered with $E = 200$ GPa and $\nu = 0.3$.

iterations is equal to 7052. This means that, in average, about only 5 iterations are required by the
 615 conjugate gradient descent method in order to converge. All considering, for a fairly large problem,
 a value of $M = 5$ gives the best numerical performances. For problems of smaller size, a value of $M \in]0, 5]$ would give the best numerical efficiency, because matrix inversion operations would be even less computationally demanding.

Appendix B. Zig-zag crack propagation in a weakly anisotropic medium

620 In Section 5.2 we analyzed the formation of a zig-zag crack path in a strongly anisotropic medium and its relation to the vector \mathbf{j} evolution. A similar analysis can be conducted for a weakly anisotropic medium as reported here.

Consider a material with weakly anisotropic fracture toughness. In this case, the anisotropic fracture toughness for each damage mechanism can for example be represented by an ellipse as shown

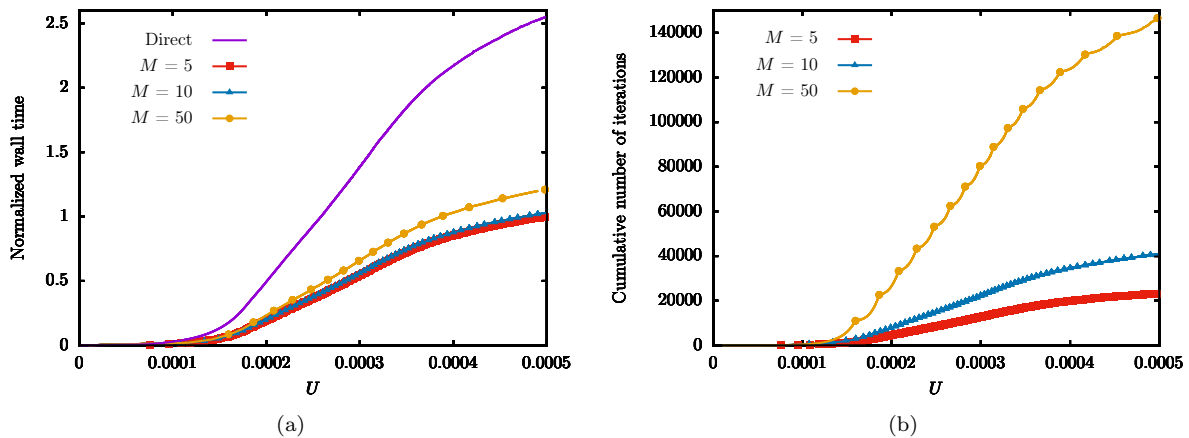


Figure A.25: (a) Normalized wall-time for direct vs hybrid resolutions. (b) Cumulative number of iterations. For hybrid resolutions, dots indicate when a direct resolution was performed.

625 in Figure B.26a. We consider a crack propagating along a slanted direction on the damage mechanism d_2 . As the crack advances, the vector \mathbf{j} rotates along the fracture toughness ellipse associated to d_2 . The component of \mathbf{j} along \mathbf{e}_x increases correspondingly. The crack propagation direction is given by the normal to the tangent where \mathbf{j} intersects this ellipse. As a consequence, the crack progressively bends towards the macroscopic propagation direction.

630 As the loading continues, the J -integral reaches the value J^* necessary to activate the fracture mechanism d_1 . Involving the nucleation of a new crack, J^* is strictly larger than the toughness G_c . This is shown as a light-red solid line in Figure B.26b at the point marked 2^- . The nucleation of the new crack is accompanied by a drop of the far-field J -integral and an instantaneous increase in fracture energy. This can for instance be observed in Figure 19 in the case $\gamma = 2$.

635 Propagation proceeds with the same phenomenology. As the vector \mathbf{j} now follows the ellipse associated to damage mechanism d_1 , the propagation direction (perpendicular to the tangent to the ellipse) bends back toward the horizontal direction. The far-field energy release rate $J_x = \mathbf{j} \cdot \mathbf{e}_x$ increases accordingly, as shown in Figure 19. Once reached the critical value $J = J^*$ at the point marked 3, a new crack is nucleated on the damage mechanism d_2 . The far-field J -integral subsequently drops in Figure 19, accompanied by an instantaneous increase in fracture energy.

640

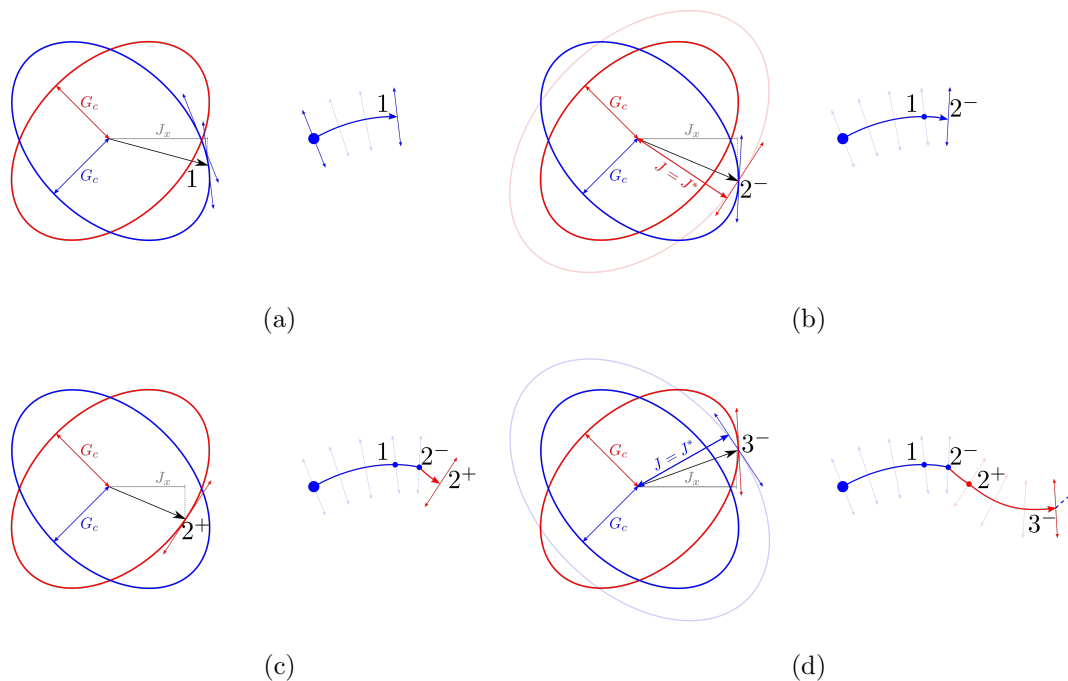


Figure B.26: Zig-zag crack paths analysis in a weakly anisotropic medium with two cleavage mechanisms.

Acknowledgements

The authors acknowledge the financial support from the Fédération Francilienne de Mécanique (project 'Coup de Pouce 2020', <https://f2m.cnrs.fr>). Computational resources at the GENCI-IDRIS center were under the Grant 2020-[A0090911874].

645 References

Alnæs, M., Blechta, J., Hake, J., Johansson, A., Kehlet, B., Logg, A., Richardson, C., Ring, J., Rognes, M.E., Wells, G.N., 2015. The fenics project version 1.5. Archive of Numerical Software 3.

- Ambrosio, L., Tortorelli, V.M., 1990. Approximation of functional depending on jumps by elliptic functional via t-convergence. *Communications on Pure and Applied Mathematics* 43, 999–1036.
- 650 Amestoy, M., Leblond, J., 1992. Crack paths in plane situations—II. Detailed form of the expansion of the stress intensity factors. *International Journal of Solids and Structures* 29, 465–501.
- Aslan, O., Cordero, N., Gaubert, A., Forest, S., 2011. Micromorphic approach to single crystal plasticity and damage. *International Journal of Engineering Science* 49, 1311–1325.
- Azhdari, A., Nemat-Nasser, S., Rome, J., 1998. Experimental observations and computational modeling of fracturing in an anisotropic brittle crystal (sapphire). *International journal of fracture* 94, 251–266.
- 655 Balay, S., Abhyankar, S., Adams, M.F., Brown, J., Brune, P., Buschelman, K., Dalcin, L., Eijkhout, V., Gropp, W.D., Kaushik, D., et al., 2001. *Petsc web page*.
- Barron, K., 1971. Brittle fracture initiation in and ultimate failure of rocks: part iii—anisotropic rocks: experimental results, in: *International Journal of Rock Mechanics and Mining Sciences & Geomechanics Abstracts*, Elsevier. pp. 565–575.
- 660 Bažant, Z.P., Pijaudier-Cabot, G., 1988. Nonlocal Continuum Damage, Localization Instability and Convergence. *Journal of Applied Mechanics* 55, 287–293.
- Bleyer, J., Alessi, R., 2018. Phase-field modeling of anisotropic brittle fracture including several damage mechanisms. *Computer Methods in Applied Mechanics and Engineering* 336, 213–236.
- 665 Bourdin, B., Francfort, G.A., Marigo, J.J., 2000. Numerical experiments in revisited brittle fracture. *Journal of the Mechanics and Physics of Solids* 48, 797–826.
- Bourdin, B., Francfort, G.A., Marigo, J.J., 2008. The variational approach to fracture. *Journal of elasticity* 91, 5–148.
- 670 Brach, S., 2020. Effects of plasticity on the anisotropy of the effective fracture toughness. *International Journal of Fracture* 226, 181–196.
- Brach, S., Hossain, M., Bourdin, B., Bhattacharya, K., 2019. Anisotropy of the effective toughness of layered media. *Journal of the Mechanics and Physics of Solids* 131, 96–111.
- Bryant, E.C., Sun, W., 2018. A mixed-mode phase field fracture model in anisotropic rocks with consistent kinematics. *Computer Methods in Applied Mechanics and Engineering* 342, 561–584.
- 675 Chaboche, J., Lesne, P., Maire, J., 1995. Continuum damage mechanics, anisotropy and damage deactivation for brittle materials like concrete and ceramic composites. *International Journal of Damage Mechanics* 4, 5–22.
- Cherepanov, G., 1967. The propagation of cracks in a continuous medium. *Journal of Applied Mathematics and Mechanics* 31, 503–512.
- 680 Clayton, J., Knap, J., 2015. Phase field modeling of directional fracture in anisotropic polycrystals. *Computational Materials Science* 98, 158–169.
- Cook, R., 2006. Strength and sharp contact fracture of silicon. *Journal of Materials Science* 41, 841–872.

- 685 De Lorenzis, L., Gerasimov, T., 2020. Numerical implementation of phase-field models of brittle fracture, in: *Modeling in Engineering Using Innovative Numerical Methods for Solids and Fluids*. Springer, pp. 75–101.
- Fassin, M., Eggersmann, R., Wulfinghoff, S., Reese, S., 2019. Gradient-extended anisotropic brittle damage modeling using a second order damage tensor–theory, implementation and numerical
690 examples. *International Journal of Solids and Structures* 167, 93–126.
- Forest, S., 2009. Micromorphic approach for gradient elasticity, viscoplasticity, and damage. *Journal of Engineering Mechanics* 135, 117–131.
- Francfort, G.A., Marigo, J.J., 1998. Revisiting brittle fracture as an energy minimization problem. *Journal of the Mechanics and Physics of Solids* 46, 1319–1342.
- 695 Gerasimov, T., De Lorenzis, L., 2022. Second-order phase-field formulations for anisotropic brittle fracture. *Computer Methods in Applied Mechanics and Engineering* 389, 114403.
- Görthofer, J., Schneider, M., Hrymak, A., Böhlke, T., 2021. A convex anisotropic damage model based on the compliance tensor. *International Journal of Damage Mechanics* , 10567895211019065.
- Hakim, V., Karma, A., 2005. Crack path prediction in anisotropic brittle materials. *Physical review
700 letters* 95, 235501.
- Hakim, V., Karma, A., 2009. Laws of crack motion and phase-field models of fracture. *Journal of the Mechanics and Physics of Solids* 57, 342–368.
- Hale, J.S., Brunetti, M., Bordas, S.P., Maurini, C., 2018. Simple and extensible plate and shell finite element models through automatic code generation tools. *Computers & Structures* 209, 163–181.
- 705 Halphen, B., Nguyen, Q.S., 1975. Sur les matériaux standard généralisés. *Journal de mécanique* 14, 39–63.
- Hossain, M., Hsueh, C.J., Bourdin, B., Bhattacharya, K., 2014. Effective toughness of heterogeneous media. *Journal of the Mechanics and Physics of Solids* 71, 15–32.
- Kachanov, L.M., 1958. Time of the rupture process under creep conditions. *Izv. Akad. Nank. SSR. Otd Tekh. Nauk* 8, 26–31.
710
- Kakouris, E., Triantafyllou, S., 2018. Material point method for crack propagation in anisotropic media: a phase field approach. *Archive of Applied Mechanics* 88, 287–316.
- Leguillon, D., 1993. Asymptotic and numerical analysis of a crack branching in non-isotropic materials. *European Journal of Mechanics. A. Solids* 12, 33–51.
- 715 Lemaitre, J., Desmorat, R., Sauzay, M., 2000. Anisotropic damage law of evolution. *European Journal of Mechanics-A/Solids* 19, 187–208.
- Li, B., Maurini, C., 2019. Crack kinking in a variational phase-field model of brittle fracture with strongly anisotropic surface energy. *Journal of the Mechanics and Physics of Solids* 125, 502–522.
- Li, B., Peco, C., Millán, D., Arias, I., Arroyo, M., 2015. Phase-field modeling and simulation of fracture
720 in brittle materials with strongly anisotropic surface energy. *International Journal for Numerical Methods in Engineering* 102, 711–727.

- Li, P., Yvonnet, J., Combescure, C., Makich, H., Nouari, M., 2021. Anisotropic elastoplastic phase field fracture modeling of 3d printed materials. *Computer Methods in Applied Mechanics and Engineering* 386, 114086.
- 725 Lindroos, M., Scherer, J.M., Forest, S., Laukkanen, A., Andersson, T., Vaarac, J., Mäntylä, Antti, Frondelius, T., 2021. Micromorphic crystal plasticity approach to damage regularization and size effects in martensitic steels. In review .
- Liu, Z., Juhre, D., 2018. Phase-field modelling of crack propagation in anisotropic polycrystalline materials. *Procedia Structural Integrity* 13, 787–792.
- 730 Logg, A., Mardal, K.A., Wells, G.N., 2012. Automated Solution of Differential Equations by the Finite Element Method: The FEniCS Book. volume 84. Springer Science & Business Media.
- Lorentz, E., Godard, V., 2011. Gradient damage models: Toward full-scale computations. *Computer Methods in Applied Mechanics and Engineering* 200, 1927–1944.
- Ma, R., Sun, W., 2020. Fft-based solver for higher-order and multi-phase-field fracture models applied to strongly anisotropic brittle materials. *Computer methods in applied Mechanics and engineering* 735 362, 112781.
- Miehe, C., Welschinger, F., Hofacker, M., 2010. Thermodynamically consistent phase-field models of fracture: Variational principles and multi-field FE implementations. *International journal for numerical methods in engineering* 83, 1273–1311.
- 740 Modniks, J., Spārniņš, E., Andersons, J., Becker, W., 2015. Analysis of the effect of a stress raiser on the strength of a ud flax/epoxy composite in off-axis tension. *Journal of Composite Materials* 49, 1071–1080.
- Mortazavian, S., Fatemi, A., 2015. Effects of fiber orientation and anisotropy on tensile strength and elastic modulus of short fiber reinforced polymer composites. *Composites part B: engineering* 72, 745 116–129.
- Munson, T., Sarich, J., Wild, S., Benson, S., McInnes, L.C., 2012. Tao 2.0 users manual. Mathematics and Computer Science Division, Argonne National Laboratory (July 2012) .
- Nguyen, Q.S., 2021. On standard gradient plasticity and visco-plasticity. *International Journal of Solids and Structures* 225, 111038.
- 750 Nguyen, T.T., Réthoré, J., Baietto, M.C., 2017a. Phase field modelling of anisotropic crack propagation. *European Journal of Mechanics-A/Solids* 65, 279–288.
- Nguyen, T.T., Réthoré, J., Yvonnet, J., Baietto, M.C., 2017b. Multi-phase-field modeling of anisotropic crack propagation for polycrystalline materials. *Computational Mechanics* 60, 289–314.
- Nguyen-Thanh, N., Li, W., Huang, J., Zhou, K., 2020. Adaptive higher-order phase-field modeling of anisotropic brittle fracture in 3d polycrystalline materials. *Computer Methods in Applied Mechanics and Engineering* 755 372, 113434.
- Noii, N., Aldakheel, F., Wick, T., Wriggers, P., 2020. An adaptive global–local approach for phase-field modeling of anisotropic brittle fracture. *Computer Methods in Applied Mechanics and Engineering* 361, 112744.

- 760 Peerlings, R.d., Borst, R.d., Brekelmans, W.d., Vree, J.d., Spee, I., 1996. Some observations on localization in non-local and gradient damage models. *European Journal of Mechanics. A, Solids* 15, 937–953.
- Pérez, R., Gumbsch, P., 2000. Directional anisotropy in the cleavage fracture of silicon. *Physical review letters* 84, 5347.
- 765 Petrini, A.L.E.R., Boldrini, J.L., Bittencourt, M.L., 2021. A thermodynamically consistent phase field framework for anisotropic damage propagation. *Latin American Journal of Solids and Structures* 18.
- Petryk, H., 2003. Incremental energy minimization in dissipative solids. *Comptes Rendus Mecanique* 331, 469–474.
- 770 Pijaudier-Cabot, G., Bazant, Z.P., 1987. Nonlocal damage theory. *Journal of engineering mechanics* 113, 1512–1533.
- Poh, L.H., Sun, G., 2017. Localizing gradient damage model with decreasing interactions. *International Journal for Numerical Methods in Engineering* 110, 503–522.
- 775 Quintanas-Corominas, A., Reinoso, J., Casoni, E., Turon, A., Mayugo, J., 2019. A phase field approach to simulate intralaminar and translaminar fracture in long fiber composite materials. *Composite Structures* 220, 899–911.
- Reese, S., Brepols, T., Fassin, M., Poggenpohl, L., Wulfinghoff, S., 2021. Using structural tensors for inelastic material modeling in the finite strain regime—a novel approach to anisotropic damage. *Journal of the Mechanics and Physics of Solids* 146, 104174.
- 780 Rezaei, S., Mianroodi, J.R., Brepols, T., Reese, S., 2021. Direction-dependent fracture in solids: Atomistically calibrated phase-field and cohesive zone model. *Journal of the Mechanics and Physics of Solids* 147, 104253.
- Rice, J.R., 1968. A Path Independent Integral and the Approximate Analysis of Strain Concentration by Notches and Cracks. *Journal of Applied Mechanics* 35, 379–386.
- 785 Riedle, J., Gumbsch, P., Fischmeister, H.F., 1996. Cleavage anisotropy in tungsten single crystals. *Physical review letters* 76, 3594.
- Scherer, J.M., Brach, S., Bleyer, J., 2021. gradam: supplementary code for "An assessment of anisotropic phase-field models of brittle fracture". doi:[10.5281/zenodo.5764329](https://doi.org/10.5281/zenodo.5764329).
- 790 Shanthraj, P., Svendsen, B., Sharma, L., Roters, F., Raabe, D., 2017. Elasto-viscoplastic phase field modelling of anisotropic cleavage fracture. *Journal of the Mechanics and Physics of Solids* 99, 19–34.
- Takei, A., Roman, B., Bico, J., Hamm, E., Melo, F., 2013. Forbidden directions for the fracture of thin anisotropic sheets: an analogy with the Wulff plot. *Physical Review Letters* 110, 144301.
- Tanné, E., Li, T., Bourdin, B., Marigo, J.J., Maurini, C., 2018. Crack nucleation in variational phase-field models of brittle fracture. *Journal of the Mechanics and Physics of Solids* 110, 80–99.
- 795 Teichtmeister, S., Kienle, D., Aldakheel, F., Keip, M.A., 2017. Phase field modeling of fracture in anisotropic brittle solids. *International Journal of Non-Linear Mechanics* 97, 1–21.
- Wu, C., McKinney, K., Rice, R., 1995. Zig-zag crack propagation in $MgAl_2O_4$ crystals. *Journal of Materials Science Letters* 14, 474–477.

- Wu, J.Y., 2017. A unified phase-field theory for the mechanics of damage and quasi-brittle failure.
800 Journal of the Mechanics and Physics of Solids 103, 72–99.
- Wulfinghoff, S., Fassin, M., Reese, S., 2017. A damage growth criterion for anisotropic damage models motivated from micromechanics. International Journal of Solids and Structures 121, 21–32.
- Wurster, S., Motz, C., Pippan, R., 2012. Characterization of the fracture toughness of micro-sized tungsten single crystal notched specimens. Philosophical Magazine 92, 1803–1825.